Consequences of Metal−Oxide Interconversion for C−H Bond Activation during CH$_4$ Reactions on Pd Catalysts

Ya-Huei (Cathy) Chin,[†,§] Corneliu Buda,[‡] Matthew Neurock,*[,‡] and Enrique Iglesia*[,†]

[†]Department of Chemical and Biomolecular Engineering, University of California, Berkeley, California 94720, United States
[‡]Departments of Chemical Engineering and Chemistry, University of Virginia, Charlottesville, Virginia 22904, United States
[§]Department of Chemical Engineering and Applied Chemistry, University of Toronto, Toronto, M5S 3E5, Canada

Ⓢ *Supporting Information*

ABSTRACT: Mechanistic assessments based on kinetic and isotopic methods combined with density functional theory are used to probe the diverse pathways by which C−H bonds in CH$_4$ react on bare Pd clusters, Pd cluster surfaces saturated with chemisorbed oxygen (O*), and PdO clusters. C−H activation routes change from oxidative addition to H-abstraction and then to σ-bond metathesis with increasing O-content, as active sites evolve from metal atom pairs (*−*) to oxygen atom (O*−O*) pairs and ultimately to Pd cation-lattice oxygen pairs (Pd^{2+}−O^{2-}) in PdO. The charges in the CH$_3$ and H moieties along the reaction coordinate depend on the accessibility and chemical state of the Pd and O centers involved. Homolytic C−H dissociation prevails on bare (*−*) and O*-covered surfaces (O*−O*), while C−H bonds cleave heterolytically on Pd^{2+}−O^{2-} pairs at PdO surfaces. On bare surfaces, C−H bonds cleave via oxidative addition, involving Pd atom insertion into the C−H bond with electron backdonation from Pd to C−H antibonding states and the formation of tight three-center (H$_3$C···Pd···H)‡ transition states. On O*-saturated Pd surfaces, C−H bonds cleave homolytically on O*−O* pairs to form radical-like CH$_3$ species and nearly formed O−H bonds at a transition state (O*···CH$_3$•···*OH)‡ that is looser and higher in enthalpy than on bare Pd surfaces. On PdO surfaces, site pairs consisting of exposed Pd^{2+} and vicinal O^{2-}, Pd$_{ox}$−O$_{ox}$, cleave C−H bonds heterolytically via σ-bond metathesis, with Pd^{2+} adding to the C−H bond, while O^{2-} abstracts the H-atom to form a four-center (H$_3$C$^{\delta-}$···Pd$_{ox}$···H$^{\delta+}$···O$_{ox}$)‡ transition state without detectable Pd$_{ox}$ reduction. The latter is much more stable than transition states on *−* and O*−O* pairs and give rise to a large increase in CH$_4$ oxidation turnover rates at oxygen chemical potentials leading to Pd to PdO transitions. These distinct mechanistic pathways for C−H bond activation, inferred from theory and experiment, resemble those prevalent on organometallic complexes. Metal centers present on surfaces as well as in homogeneous complexes act as both nucleophile and electrophile in oxidative additions, ligands (e.g., O* on surfaces) abstract H-atoms via reductive deprotonation of C−H bonds, and metal−ligand pairs, with the pair as electrophile and the metal as nucleophile, mediate σ-bond metathesis pathways.
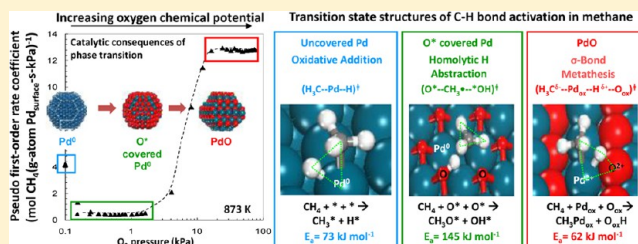
1. INTRODUCTION

Phase transitions among metals and their oxides, sulfides, or carbides occur as the respective chemical potentials of oxygen, sulfur, or carbon vary with temperature and with the concentrations of the reactant and product molecules that contain these heteroatoms. These phase transitions lead to significant catalytic consequences, as shown for CH$_4$ oxidation,[1] hydrodesulfurization,[2,3] and Fischer−Tropsch synthesis[4] catalysis. Specifically Pd−PdO transitions during catalytic CH$_4$−O$_2$ reactions have shown how turnover rates can increase abruptly as Pd clusters undergo bulk oxidation with increasing O$_2$/CH$_4$ ratio or decreasing temperature;[5] these interconversions lead to hysteresis in CH$_4$ oxidation rates with changes in temperature and oxygen chemical potential.[6,7] Such hysteresis behavior prevents unequivocal connections between the observed catalytic behavior and the thermodynamics of Pd−PdO transitions as well as rigorous interpretations of the effects of cluster size on the relative reactivity and stability of the metal and oxide phases. The fact that oxygen chemical potentials at surfaces reflect the kinetic coupling of the steps that remove chemisorbed oxygens (O*) and form them via O$_2$ dissociation (and not just the thermodynamics of the latter step), and the ubiquitous effects of temperature and concentration gradients for such fast exothermic reactions have made rigorous interpretations of these catalytic consequences of phase transitions a formidable and still largely unresolved challenge.

In our studies, we have removed transport artifacts by extensive dilution and established the reversible nature of Pd−PdO interconversions during CH$_4$−O$_2$ catalysis,[8] thus ensuring the chemical origins of measured turnover rates and the thermodynamic nature of the phase transitions. These data, taken together with isotopic experiments and density functional theory (DFT) calculations, have led to rigorous mechanistic interpretations of CH$_4$−O$_2$ reactions on the surfaces of PdO and Pd metal clusters sparsely covered or saturated with
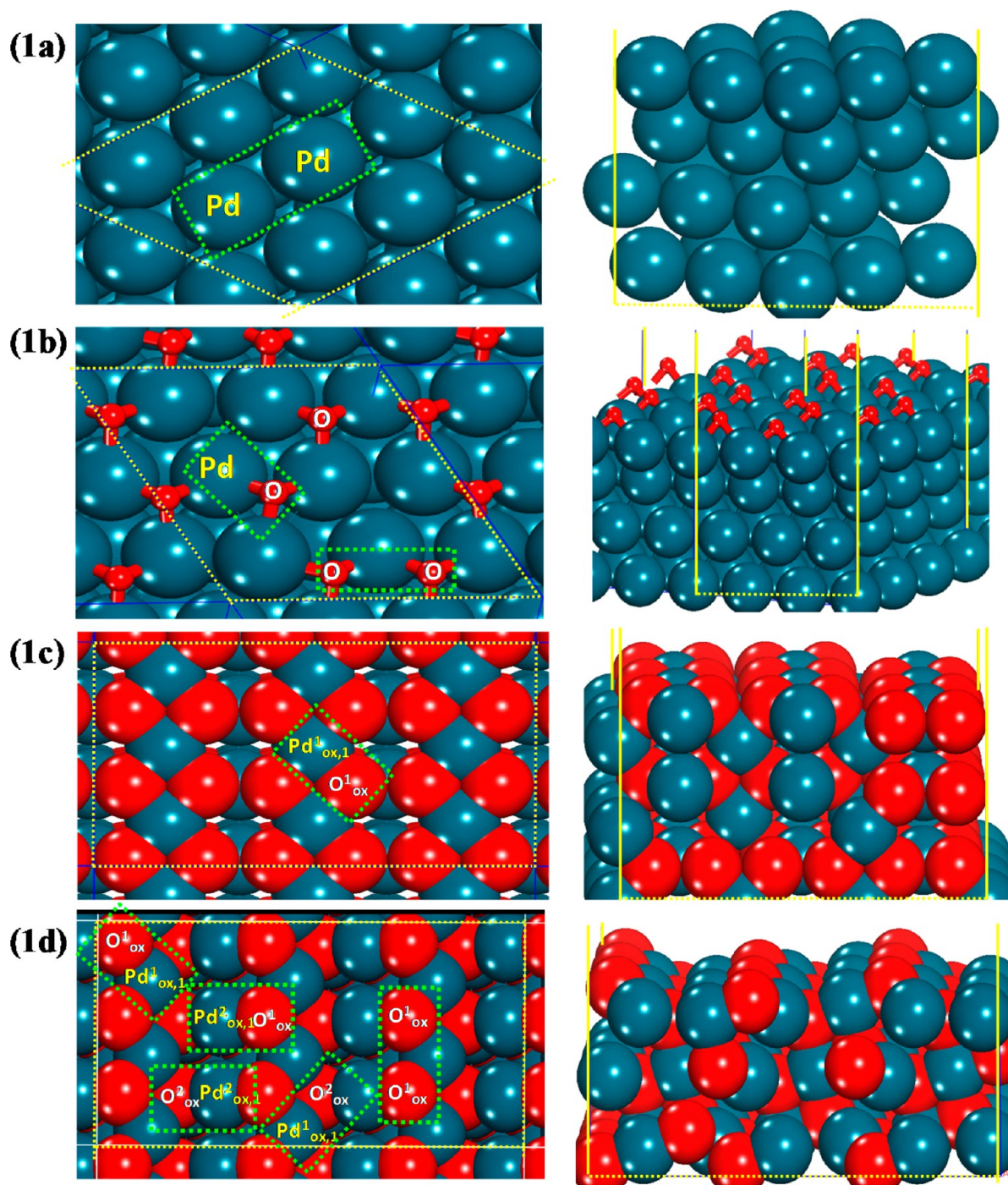
Figure 1. DFT-optimized models of (a) Pd(111), (b) 0.67 ML O*-covered Pd(111), (c) PdO(100), and (d) PdO(101) single crystal surfaces used to examine the activation of methane. The Pd atoms and O atoms are shown in blue and red, respectively. Pd–Pd site pair (in 1a), Pd–O* and O*– O* site-pairs (in 1b), nonstoichiometric Pd_{ox}–O_{ox} site-pair (labeled $Pd^1_{ox,1}$–O^1_{ox} in 1c), and stoichiometric Pd_{ox}–O_{ox} (labeled $Pd^2_{ox,1}$–O^1_{ox}, $Pd^2_{ox,1}$– O^2_{ox} in 1d), nonstoichiometric Pd_{ox}–O_{ox} (labeled $Pd^1_{ox,1}$–O^1_{ox}, $Pd^1_{ox,1}$–O^2_{ox} in 1d) and O_{ox}–O_{ox} site pairs (and O^1_{ox}–O^1_{ox} in 1d) are boxed in green. The sites involving O^2_{ox} are not considered as the four-coordinate O^2_{ox} centers are inaccessible. The yellow lines in each model define the unit cell used in DFT calculations.

chemisorbed O*. These insights build on earlier proposals for the sequence of elementary steps that mediate CH_4–O_2 catalysis on Pd[9] and Pt clusters[10] and C_2H_6–O_2[11] catalysis on Pt clusters and on the known effects of O* coverage and binding energy on the nature and effectiveness of the sites required for C–H bond activation.

We show here that the activation of the first C–H bond in CH_4 is the kinetically relevant step on sparsely covered and O*-

saturated Pd metal clusters and on PdO clusters and that such steps evolve from oxidative addition, to H-abstraction, and ultimately to σ-bond metathesis, each with distinct transition-state structures, as the oxygen chemical potential increases. These diverse C–H bond activation paths evolve in response to differences in the charge and accessibility of oxygen species [chemisorbed oxygen atom (O*) on Pd; lattice oxygen (O_{ox}) on PdO] and Pd centers (Pd^0 or Pd^{2+}) and in their respective

15426

dx.doi.org/10.1021/ja405004m | J. Am. Chem. Soc. 2013, 135, 15425–15442

interactions with the CH_3 and H moieties that incipiently form at C−H activation transition states, which determine, in turn, activation free energies and rates. Metal centers activate the C−H bond serving as both the nucleophile and electrophile during the oxidative addition on Pd^0 sites at Pd surfaces, chemisorbed oxygen atoms (O*) activate the C−H bond in a H-abstraction step involving the reductive deprotonation of the C−H bond on O*-saturated Pd^0 surfaces, and metal and ligand pairs $(Pd^{2+}-O^{2-})$ activate the C−H bond in a concerted path where the metal acts as the nucleophile and the metal−ligand pair as the electrophile in a σ-bond metathesis step. These mechanistic bases seem also generally applicable to C−H bond activation on surfaces of sulfides, carbides, and nitrides and resemble that on organometallic complexes. The mechanistic synergies illustrated here in heterogeneous and homogeneous catalysis provide a rigorous description for the ubiquitous C−H bond activation paths in both systems.

2. METHODS

2.1. Catalyst Synthesis. Pd/Al_2O_3 (0.2 % wt) was prepared by incipient wetness impregnation of γ-Al_2O_3 (Sasol North America Inc., lot no. C1643, 193 m^2 g^{-1}, 0.57 cm^3 g^{-1} pore volume) with aqueous solutions of $Pd(NO_3)_2$ (Aldrich, 99.999% purity, 10 % wt $Pd(NO_3)_2$ in 10 % wt HNO_3). The γ-Al_2O_3 was treated in flowing dry air (Praxair, zero grade, 60 cm^3 g^{-1}) by heating to 1073 K at 0.083 K s^{-1} and holding for 5 h before the impregnation step. Impregnated powders were treated in stagnant ambient air at 383 K for >4 h. These samples were then treated in flowing dry air (60 cm^3 g^{-1}) by heating to 623 K at 0.033 K s^{-1} and holding for 3 h and then to 1073 K at 0.083 K s^{-1} and holding for 10 h, before cooling to ambient temperature. These samples were finally treated in a flowing H_2−He mixture (5 kPa H_2, Praxair, UHP grade H_2 and He, 60 cm^3 g^{-1}) to 1023 K (at 0.083 K s^{-1}) and held for 5 h, cooled in He to ambient temperature, and passivated by exposing samples to a flowing 0.5% O_2/He mixture (0.5% O_2/He, Praxair, certified standard, 30 cm^3 g^{-1}) for 2 h. These catalyst powders were mixed with SiO_2 (Davison Chemical, grade 923, CAS no. 112926-00-8, 280 m^2 g^{-1}) to give a SiO_2/catalyst mass ratio of 200 and subsequently pelleted and sieved to retain 106−250 μm aggregates. The Pd dispersion (the fraction of Pd atoms residing at cluster surfaces) in these samples was determined from irreversible O_2 chemisorption uptakes (1:1 O:$Pd_{surface}$) at 313 K, measured in a volumetric adsorption apparatus (Autosorb-1, Quantachrome) on samples treated at 673 K in flowing H_2 (30 cm^3 g^{-1}) for 2 h. The mean cluster size was estimated from these dispersion values by assuming hemispherical Pd clusters with the atomic density of bulk Pd metal (12.0 g cm^{-3}).[12]

2.2. Steady-State Catalytic Rate Measurements. Catalyst aggregates (Pd/Al_2O_3 and SiO_2 mixtures, 0.12−0.5 g, SiO_2-to-Pd/Al_2O_3 mass ratio of 200) were physically mixed with quartz powder (Fluka, product no. 84880, 106−250 μm diameters) at quartz-to-Pd/Al_2O_3 mass ratios of 200−1200 to avoid intraparticle and bed gradients in temperature or concentration. The quartz powder, SiO_2 diluents (Davison Chemical, grade 923, CAS no. 112926-00-8, 280 m^2 g^{-1}), and Al_2O_3 support did not give detectable rates at any of the reaction conditions used. The catalyst and diluent mixtures were held on a quartz frit within a quartz tubular reactor (8.1 mm ID) with plug-flow hydrodynamics and operated differentially. Bed temperatures were measured with a K-type thermocouple held within a concentric quartz thermowell located at the center of the catalyst bed. All samples were treated in 5% H_2/He (1.67 cm^3 s^{-1}) by heating to reaction temperatures of 800−975 K at 0.083 K s^{-1} and then in flowing He (1.67 cm^3 s^{-1}) before exposure to CH_4−O_2 reactants.

Reactant mixtures were prepared by mixing 25% CH_4/He (Matheson, certified plus grade) with pure O_2 (Praxair, UHP grade) or 5% O_2/He (Praxair, certified standard grade) and with He (Praxair, UHP grade) using electronic mass flow controllers (Porter 201). CH_4, O_2, and CO_2 concentrations in the inlet and outlet streams were measured by gas chromatography (Agilent 3000A Micro GC,

equipped with PoraPLOT Q or Mol Sieve 5A columns connected to thermal conductivity detectors). CH_4 conversion turnover rates were determined from effluent CO_2 concentrations, and the number of exposed Pd atoms determined from O_2 chemisorption. Heat and mass transport corruptions on rate data reported here were ruled out from turnover rate data that did not depend on intrapellet and bed dilution ratios,[13] as reported elsewhere.[9]

2.3. Ab initio Density Functional Methods. The structures and energies of the reactant, transition, and product states in CH_4−O_2 reactions on Pd(111), 2/3 ML O*-covered Pd(111) [hereinafter ML denotes monolayer], PdO(100), and PdO(101) single crystal surfaces shown in Figure 1a−d and 1 ML O*-covered clusters of 201 Pd atoms (denoted as O*/Pd_{201}) and PdO clusters of 183 atoms ($Pd_{94}O_{89}$) shown in Figure 2a,b were calculated using periodic plane-wave DFT
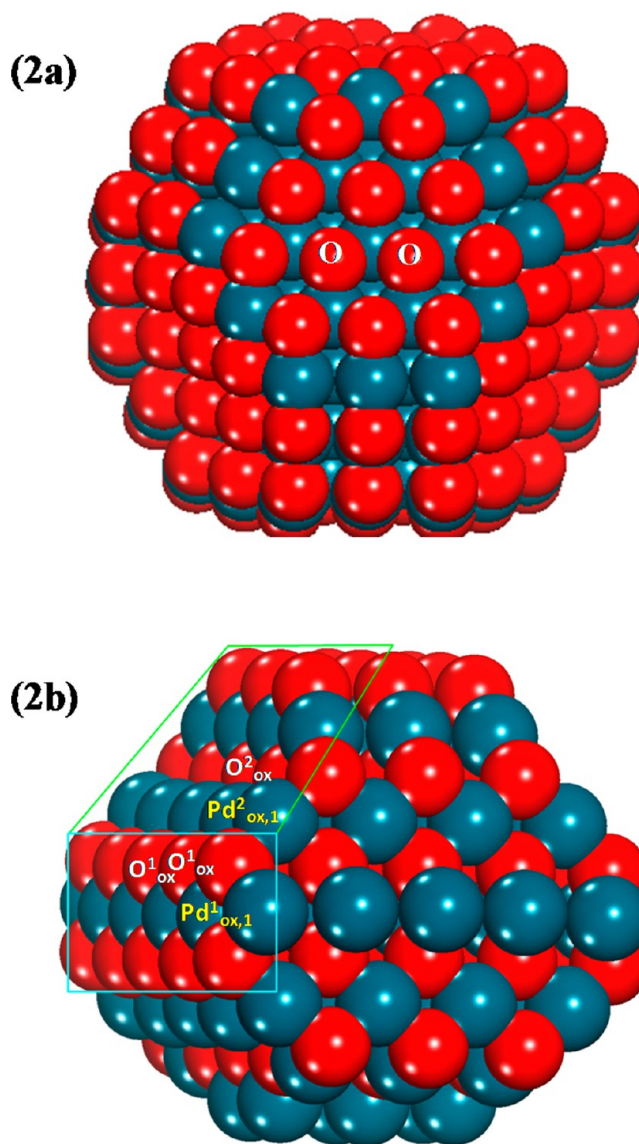
Figure 2. DFT-optimized model of cuboctahedral 1 ML O*-covered Pd and PdO clusters used to examine the activation of methane. (a) 1 ML O*-covered Pd_{201} and (b) 183 atom PdO ($Pd_{94}O_{89}$) clusters. The Pd and O atoms are shown in blue and red, respectively. The (100) and (101) facets on $Pd_{94}O_{89}$ cluster are highlighted in blue and green, respectively. The nonstoichiometric Pd_{ox}−O_{ox} (labeled $Pd^1_{ox,1}$−O^1_{ox}), the stoichiometric Pd_{ox}−O_{ox} (labeled $Pd^2_{ox,1}$−O^1_{ox}) and the O_{ox}−O_{ox} site pairs (labeled O^1_{ox}−O^1_{ox}) are the only sites considered as the sites involving the four-coordinate O^2_{ox} sites are inaccessible. Note that O^1_{ox} atoms are shared between PdO(100) and PdO(101) facets.

methods, as implemented in the Vienna ab-initio simulation program (VASP).[14−16] The ideal single crystal Pd(111), PdO(100), and PdO(101) surfaces were used to elucidate the mechanisms and understand the charge-transfer processes that occur along the reaction coordinate, whereas the more realistic 1 ML O*-covered Pd_{201} and $Pd_{94}O_{89}$ clusters were used to confirm the results from the ideal surfaces and provide more reliable energies. All calculations were carried out spin-polarized within the generalized gradient approximation (GGA) using the Perdew−Wang 91 (PW91)[13] exchange−correlation potential and ultrasoft pseudopotentials (US-PP) to describe interactions between core and valence electrons.[17] Wave functions were constructed from periodic plane-wave expansions out to a kinetic energy cutoff of 396 eV. A $3 \times 3 \times 1$ Monkhorst−Pack k-point mesh was used to sample the first Brillouin zone.[18] The wave functions were converged to a tolerance of 10^{-4} eV, while the geometric structures were optimized until forces on each atom were <0.5 eV nm^{-1}. The occupancies of the wave functions were determined using the second-order Methfessel−Paxton method[19] to smear out discontinuities over an energy width of 0.2 eV.

Pd(111) surfaces (Figure 1a) were modeled using a 3×3 unit cell consisting of four Pd atom layers, each with nine Pd atoms per layer and a 1 nm thick vacuum region above the surface; this configuration avoids interactions between atoms in adsorbates at Pd surfaces and Pd atoms at the bottom of the next slab. The lattice constant obtained with PW91 functionals and ultrasoft pseudopotentials was 0.395 nm, in agreement with experimental values (0.389 nm).[20] The active Pd−Pd site pairs are labeled in Figure 1a, Pd−O* and O*−O* in Figure 1b, Pd_{ox}−O_{ox} in Figure 1c, and Pd_{ox}−O_{ox} and O_{ox}−O_{ox} in Figure 1d. C−H bond activation barriers on four-layer Pd(111) slabs, in which the top two layers were allowed to relax and the bottom two layers were kept at either the experimental or the DFT-derived distances, differed by <5 kJ mol^{-1}. In the calculations on Pd clusters [bare cubocahedral Pd_{201}, O*-covered cuboctahedral Pd_{201} (Figure 2a)] and PdO clusters ($Pd_{94}O_{89}$, Figure 2b), the clusters were placed in the center of the $3 \times 3 \times 3$ nm^3 unit cell with minimum distances of at least 0.8 nm between each of the cell edges. All of the atoms of the cluster were allowed to fully optimize subject to the same electronic and geometric convergence criteria outlined above for the surfaces.

In order to model the charge transfer processes that occur as methane is activated on the oxygen−oxygen (O*−O*) and Pd-oxygen atom (*−O*) site pairs on O*-covered Pd clusters, we have examined the reactivity of methane on ideal Pd(111) surfaces with different O*-coverages as presented in the Supporting Information. The 2/3 ML O* (see Figure 1b) was chosen as a simple model of the O*-saturated surface as it resulted in the maximum O* coverage on Pd(111) with the lowest negative differential enthalpy over a surface that did not reconstruct. We recognize that such coverages cannot be realized experimentally on single crystal surfaces as these surfaces reconstruct for coverages greater than 1/4 monolayer of O*[21] in order to accommodate the strain from the increased repulsion in the O* adlayer. Supported metal clusters, however, can achieve surface coverages of 1 ML O* without converting to an oxide as they can expand radially to remove strain (Figure 2a). We use here an ideal Pd(111) model surface with 2/3 ML O* to monitor charge transfer along the reaction coordinate. Such a simple model seems reasonable because C−H activation on O*-covered Pd surfaces depends only on the binding and reactive properties of each O-atom, without any effects of distances to vicinal Pd or O atoms (evidence in Sec. 3.2), making transition-state structures and mechanistic interpretation insensitive to the detailed structure of O*-covered surfaces. The optimized structures of the reactant, transition, and product states as well as the activation energies for C−H bond dissociation in methane were also calculated over O*-covered Pd_{201} clusters which accommodate up to 1 ML O* to provide a more faithful model of the working O*-covered Pd catalysts used herein.

The activation of the first C−H bond of CH_4 was also examined on PdO(100) and PdO(101) surfaces which are reported to be the most stable PdO surfaces.[22] These surfaces were constructed using a 3×3 PdO unit cell consisting of 32 Pd and 32 O atoms with a 1 nm vacuum gap between slabs. The PdO(100) surface is comprised of alternating

parallel layers of Pd and PdO_2 as shown in Figure 1c, thus resulting in an overall stoichiometry of PdO. The exposed (100) surface layer is PdO_2 in character and thus nonstoichiometric where each Pd atom binds to 3 Pd and 4 O neighbors and each oxygen bonds to 3 Pd atoms (2 in the surface and 1 subsurface). These nonstoichiometric Pd and O surface atoms are labeled as $Pd^1_{ox,i}$ and as O^1_{ox}, where the superscript 1 specifies that these are nonstoichiometric surface atoms and the subscript i on the Pd_{ox} refers to the specific Pd atom where 1 refers to the active Pd center and 2 and 3 refer to nearest-neighbor Pd sites which are used only to aid in charge analysis. The PdO(101) surface is comprised of alternating planes that run parallel to the diagonal of the unit cell which is depicted in Figure 1d. These alternating planes are comprised of stoichiometric Pd centers (site $Pd^2_{ox,i}$) that are bound to 2 Pd and 3 O nearest neighbors and nonstoichiometric Pd centers (site $Pd^1_{ox,i}$) with 3 Pd and 4 O neighbors, respectively. The PdO(101) surface is comprised of the two different oxygen atom types labeled O^1_{ox} and O^2_{ox} in Figure 1d. The O^1_{ox} site sits within the PdO(100) plane and is thus identical to the O^1_{ox} sites of the PdO(100) surface. The O^2_{ox} site which has 4 Pd nearest neighbors and sits subsurface is considered inactive. The Pd and O atoms in the bottom three layers of both the PdO(100) and PdO(101) slabs were held fixed at their bulk lattice positions (0.202 nm interatomic distance between Pd^{2+} and O^{2-},)[23] while the three outer layers and any adsorbed species were fully optimized using the same convergence criteria as for Pd(111). The PdO surfaces and clusters were modeled using standard GGA approach presented above. The Hubbard U parameter is typically used as a correction to account for the correlation of d and f electron that is not considered in standard DFT methods. These corrections are required to describe electronic transitions between valence and conduction bands and reduction−oxidation reactions in oxides with d and f electrons, as such processes involve electron transfer between two very different environments as a result of the concomitant changes in the oxidation state of the metal centers. Previous studies[24] have shown that GGA+U simulations (with U = 7 eV) give accurate band gaps for bulk PdO but do not significantly influence adsorption energies for H_2O and OH on PdO. We show here that there are no changes in oxidation state for Pd or O atoms in PdO along the reaction coordinate and that C−H activation involves the heterolytic splitting of the C−H bond, where the negative charge accumulates on the methyl fragment instead of the Pd atom (Figure 12). Thus, we do not expect any effects of introducing a U parameter. Indeed, the barriers for C−H bond activation on PdO(101) and PdO(100) surfaces with and without U (7 eV) differed by <2 and <1 kJ mol^{-1}, respectively.

All transition states reported herein were isolated using the nudged elastic band (NEB)[25] method to find the lowest-energy path along a sequence of steps from the reactant to the transition state and subsequently refined using climbing image-nudged elastic band (CI-NEB) methods.[26−28] The NEB approach was used to identify the highest-energy image along the reaction coordinate and to determine the forces on this structure. These forces were subsequently used to maximize the energy of this structure along the reaction coordinate while minimizing the energy of this structure along all other modes.[9] Transition-state structures were considered to have converged when forces on all atoms were <0.5 eV nm^{-1}. All activation barriers are reported as the difference in energy between the C−H activation transition state and CH_4(g), because such values reflect the relevant barriers determined from rate data. Zero-point energy corrections at 873 K decreased activation barrier for the initial C−H bond activation in methane by <6 kJ mol^{-1} on Pd(111) and similar small effects are expected on the other surfaces.

The charges on all surface atoms along the reaction coordinate were calculated using Bader charge methods,[29] which split the charge density in the region between two atoms along a plane that is perpendicular to the connecting line between the two atoms and shows a minima in charge density. Such an approach provides essential mechanistic insights into the role of Pd and O surface species in C−H bond activation, but as in the case of all charge analysis formalisms, it cannot rigorously or unequivocally apportion the actual charges at any one atom.

3. RESULTS AND DISCUSSION

3.1. Kinetically Relevant Steps in CH_4-O_2 Reactions on Surfaces of Pd and PdO Clusters.

Turnover rates for CH_4-O_2 reactions were measured over a broad range of O_2 (0.15–87 kPa) and CH_4 (0.8–4.8 kPa) pressures at 873 K. Figure 3 shows the effect of O_2 pressure on pseudo-first-order
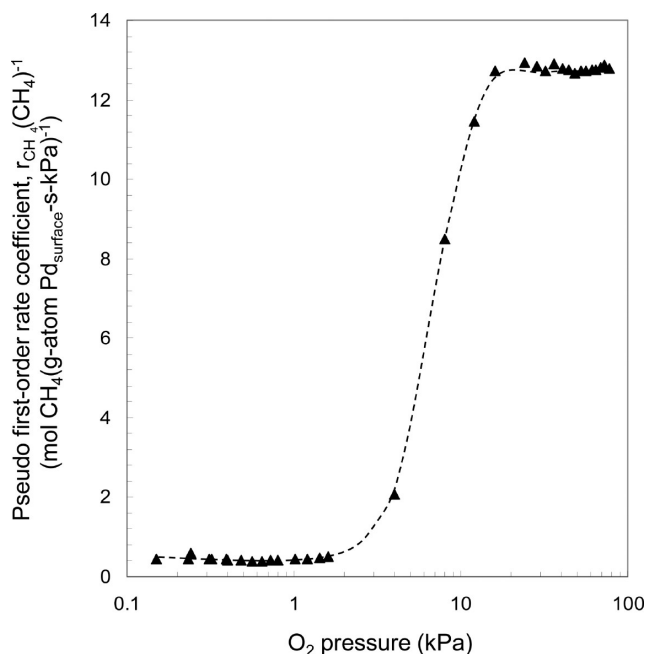
Figure 3. Reactive CH_4 collision probabilities, also the pseudo-first-order rate coefficients ($r_{CH_4}(CH_4)^{-1}$), on 0.2 % wt Pd/Al_2O_3 (21.3 nm mean Pd cluster diameter determined at the metallic state) as a function of O_2 pressure at 873 K. ($0.94-3.92 \times 10^9$ cm^3 (s mol $Pd_{surface})^{-1}$; 200 SiO_2/catalyst intraparticle dilution ratio; 200 and 1200 quartz/catalyst interparticle dilution ratio for O_2 pressures below and above 4 kPa, respectively).

rate coefficients, defined as the turnover rates divided by the CH_4 pressure ($r_{CH_4}(CH_4)^{-1}$), on Pd/Al_2O_3 (0.2 % wt Pd, 21.3 nm mean Pd cluster diameter) at differential CH_4 conversions (<1.5%). Similar effects of O_2 pressure on rate coefficients were reported at higher temperatures, but the sharp increase in rate coefficients occurred at higher O_2 pressures (1.7 kPa at 873 K and >35 kPa at 973 K) than at the lower temperatures of the current study. Such transitions reflect the interconversion of Pd to PdO, as we show next, and these temperature effects show that the Pd–PdO phase boundary moves to higher oxygen chemical potentials as temperature increases, as expected from the exothermic nature of the Pd oxidation reaction.

These rate coefficients did not vary with time, indicating that Pd clusters and their surfaces did not reconstruct during steady-state catalysis; active sites and their reactivity were constant throughout all catalytic measurements.[30] No CO or H_2 was detected (0.15–73 kPa O_2, 4.85 kPa CH_4, 873 K), even at the lowest O_2 pressures, indicating that catalytic partial oxidation did not occur at detectable rates at conditions of rigorous kinetic control. These conclusions were confirmed by the much higher reactivity of ^{12}CO compared with $^{13}CH_4$ on Pd clusters,[9] as also found for CH_4-O_2[31] and $C_2H_6-O_2$[11] reactions on Pt catalysts. Such data preclude the formation and removal of CO from the catalyst bed in the presence of O_2. At low O_2 pressures (<1.7 kPa), pseudo-first-order rate coefficients remained

constant with O_2 pressure (Figure 3). In this regime, the effects of CH_4 and O_2 pressure were consistent with turnover rates proportional to CH_4 pressure and independent of O_2 pressure (Figure 4a). These data, taken together with measured CH_4/CD_4 kinetic isotope effects (KIE = 2.01 at 873 K; Table 1), indicate that the activation of the first C−H bond in CH_4 is the sole kinetically relevant step and that this step occurs on Pd cluster surfaces saturated with chemisorbed oxygen atoms (O*). The rates of $^{16}O^{18}O$ formation with $CH_4-^{16}O_2-^{18}O_2$ and $^{16}O_2-^{18}O_2$ reactant mixtures were identical within experimental accuracy.[9] These similar $^{16}O-^{18}O$ isotopologue formation rates with $CH_4-^{16}O_2-^{18}O_2$ (O_2 <1.7 kPa) and with $^{16}O_2-^{18}O_2$ (at chemical equilibrium) mixtures show that chemisorbed O* species are present at similar coverages in the presence and absence of CH_4 and that O* species remain in quasi-equilibrium with $O_2(g)$ during CH_4-O_2 reactions. Therefore, oxygen chemical potentials at Pd cluster surfaces depend only on $O_2(g)$ pressures and are unaffected by the presence of reactants or products (CH_4, CO_2, and H_2O); these chemical potentials rigorously represent the thermodynamic driving force for all surface or bulk transformations of Pd clusters. As a result, the O* content in Pd clusters during catalysis can be determined rigorously from O_2 chemisorption uptakes at the O_2 pressures and temperatures of catalysis but without the concurrent presence of CH_4.

Volumetric O_2 uptakes were used to measure O/Pd atomic ratios and to determine the extent to which Pd clusters covered with O* species and ultimately form bulk PdO with increasing oxygen chemical potentials. At 873 K and low O_2 pressures (<7.5 kPa), O/Pd_{total} atomic ratios (Pd_{total} denotes the total number of Pd atoms) were similar to those measured at near ambient temperatures (313 K), which prevent bulk dissolution and retain O* species at surfaces with an adsorption stoichiometry of unity [(O/$Pd_{surface})_{313K} = 1$; $Pd_{surface}$ denotes Pd atoms at cluster surfaces]. The O/Pd_{total} ratios at near ambient temperature indicate that the fractional Pd dispersion of this sample is 0.047 [(O/$Pd_{total})_{313K} = Pd_{surface}/Pd_{total} = 0.047$], corresponding to a 21.3 nm mean cluster diameter.[9] This value, taken together with the O/Pd_{total} ratios at 873 K, give an O/$Pd_{surface}$ ratio of 1.06 at 873 K, indicating that clusters retain their metallic bulk during CH_4 oxidation catalysis, but their surfaces are saturated with O* with traces of oxygen possibly dissolved in their bulk.

At O* saturation coverages, the dearth of uncovered Pd atoms (*) causes C−H activation steps to require the involvement of O* in H-abstraction steps, without the concerted involvement of Pd atoms in stabilizing the CH_3 groups formed. These CH_3 groups retain radical-like character in the transition state and ultimately bind to another O* to form bound methoxy species as the products of the C−H activation elementary step. Therefore, the dynamics and specifically the free energy of activation of this kinetically relevant step depend on the thermochemical properties of O*, as proposed and confirmed by kinetic and isotopic studies of alkane oxidation reactions (CH_4[10] and C_2H_6[11]) on Pt clusters and consistent with DFT-derived activation energies for C−H cleavage on O*−O* site pairs at oxygen-saturated surfaces of Pt[10] and Pd clusters in cuboctahedral shape with 201 metal atoms and at oxygen saturated Pd(111) surfaces (where 2/3 ML O* is used to mimic saturation on Pd(111)), as shown in Section 3.2.

Rate coefficients increased markedly with increasing O_2 pressure (above ~3 kPa) and ultimately reached nearly

15429

dx.doi.org/10.1021/ja405004m | *J. Am. Chem. Soc.* 2013, 135, 15425−15442
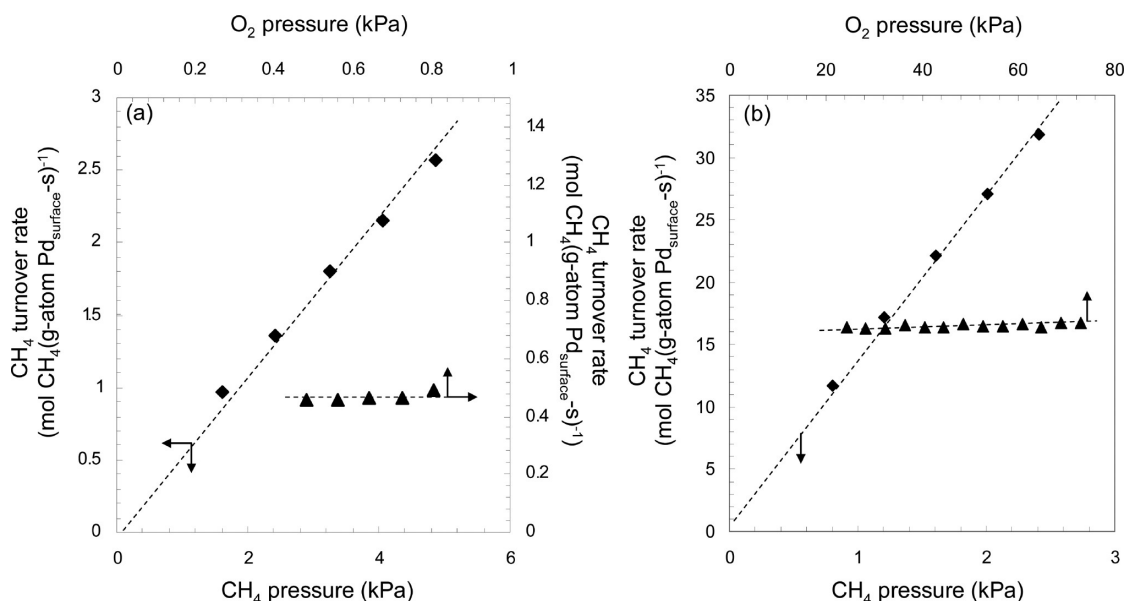
Figure 4. (a,b) CH_4 conversion turnover rates as a function of CH_4 (◆) and O_2 (▲) pressures on 0.2 % wt Pd/Al_2O_3 (21.3 nm mean Pd cluster diameter determined at the metallic state) at 873 K in the range of oxygen chemical potential that led to clusters in metallic Pd (a) or PdO (b) phase. Oxygen chemical potential during catalysis is given by the O_2 pressures on O* covered metallic Pd clusters, as shown elsewhere[9] but by the O_2/CH_4 ratios on PdO cluster surfaces; space velocity $0.94-3.92 \times 10^9$ cm^3 (s mol $Pd_{surface}$)$^{-1}$; 200 SiO_2/catalyst intraparticle dilution ratio; 200 and 1200 quartz/catalyst interparticle dilution ratio for O_2 pressure below and above 4 kPa, respectively; ◆: 0.48 and 77 kPa O_2 on Pd (a) and PdO (b) clusters, respectively; ▲: 1.0 and 1.2 kPa CH_4 on Pd (a) and PdO (b) clusters, respectively.
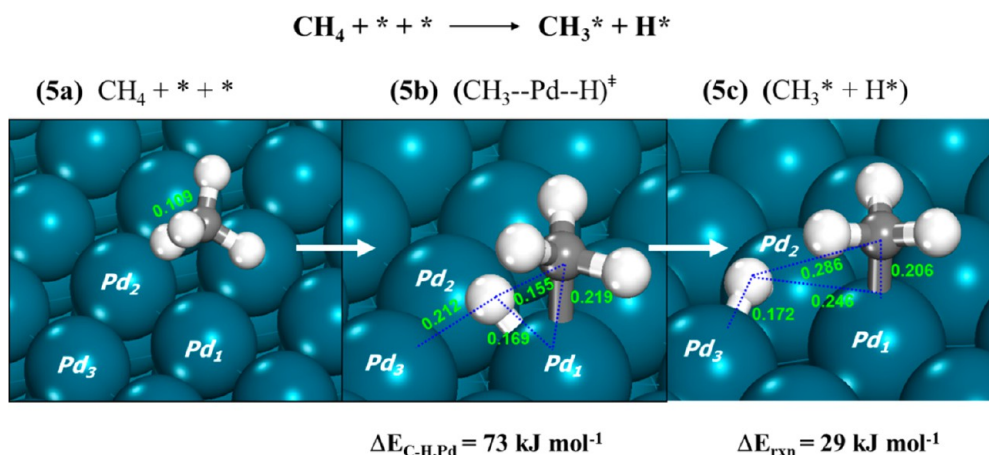
Table 1. Measured C−H/C−D Kinetic Isotope Effects, Activation Barriers and Entropies, and DFT-Derived Activation Barriers for C−H Bond Activation in CH_4 on Pd Metal, O*-Covered Pd Metal, and PdO Clusters and Surfaces

	catalysts	active sites	C−H/C−D KIEs	activation barrier (kJ mol^{-1})	pre-exponential factor (experiment) (kPa^{-1} s^{-1})	activation entropy[e] (J mol^{-1} K^{-1})	activation barrier (theory) (kJ mol^{-1}) on extended surfaces	on clusters
Pd[a]	1.6 % wt Pd/ZrO_2 (12.5 nm Pd clusters)[d]	*−*	1.41 (823K)	84	4×10^5	−125	73[f]	68
O*/Pd[b]	0.2 % wt Pd/Al_2O_3 (21.3 nm Pd clusters)[d]	O*−O*	2.01 (873 K)	158	1.5×10^9	−57	145[g] (0.67 ML O*)	141[h]
		−O	u.d.	u.d.	u.d.	u.d.	117[g] (0.67 ML O*) 133[j] (0.11 ML O*)	96[i] (0.985 ML O*) 131[k] (0.995 ML O*)
PdO[c]	0.2 % wt Pd/Al_2O_3	$Pd_{ox}−O_{ox}$	1.99 (873 K)	61	1.4×10^5	−134	62[l]	61[m]
	(21.3 nm Pd clusters)[d]	$O_{ox}−O_{ox}$					196[l]	−
		$Pd_{ox}−O_{ox}$					131[n]	−

[a]From ref 32, measured in $CH_4−CO_2$ mixtures. [b]1.2−1.6 kPa O_2. [c]72 kPa O_2. [d]Nominal mean cluster diameters, estimated based on Pd in metallic state with the assumption of an oxygen-to-exposed Pd atomic ratio of one and hemispherical Pd cluster shapes. [e]Measured entropy changes required for CH_4(g) to form the C−H activation transition-state complexes. [f]Pd(111) surfaces. [g]0.67 ML O* covered Pd(111) surfaces. [h]O* covered Pd(111) surfaces of the 1 ML O* covered cuboctahedral Pd clusters with 201 Pd atoms. [i]O* covered Pd(111) surfaces of the 0.985 ML O* covered cuboctahedral Pd clusters with 201 Pd atoms (three oxygen vacancies). [j]0.11 ML O* covered Pd(111) surfaces. [k]O* covered Pd(111) surfaces of the 0.995 ML O* covered cuboctahedral Pd clusters with 201 Pd atoms (one oxygen vacancies). [l]PdO(101) surfaces. [m]PdO(101) surfaces of the 183 atom PdO ($Pd_{94}O_{89}$) cluster. [n]PdO(100) surfaces. u.d.: *−O* sites are undetectable experimentally at the temperature and oxygen chemical potential range used for the rate measurements reported herein.

constant values (12.9 mol CH_4 (g-atom $Pd_{surface}$-kPa-s)$^{-1}$, 873 K) at 15−80 kPa O_2 (Figure 3). This sharp kinetic transition coincides with the conversion of O*-saturated Pd metal clusters to PdO, during which oxygen atoms incipiently dissolve into the cluster bulk. Pd clusters concurrently expand, and the oxidation state of Pd atoms increases, driven by thermodynamics, as oxygen chemical potentials (set by the prevalent O_2 pressures) increase. These transitions and their kinetic consequences have been previously reported for Pd foils[1] and dispersed Pd clusters[5] and coincide with an increase in O_2 uptakes, which exceed saturation levels and approach the expected O content of bulk PdO (O/Pd_{total} ratio = 0.98, as reported elsewhere).[8] The higher rates that coincide with this phase transition did not lead to changes in the rate dependencies of CH_4 and O_2 pressures or in the measured values of C−H/C−D kinetic isotope effects (KIE), which remained similar to those for Pd metal clusters saturated with O* (Figure 4a,b; KIE values of 1.99 (PdO) and 2.01 (O*/Pd)

$$\text{CH}_4 + * + * \longrightarrow \text{CH}_3* + \text{H}*$$

(5a) $\text{CH}_4 + * + *$ **(5b)** $(\text{CH}_3\text{--Pd--H})^{\ddagger}$ **(5c)** $(\text{CH}_3* + \text{H}*)$

$\Delta\text{E}_{\text{C-H,Pd}} = 73 \text{ kJ mol}^{-1}$ $\Delta\text{E}_{\text{rxn}} = 29 \text{ kJ mol}^{-1}$

Figure 5. DFT-calculated structures of reactant (**5a**), transition (**5b**), and product (**5c**) states and energy changes (in kJ mol^{-1}; with respect to the energy of gas phase CH$_4$) for C−H bond activation steps on Pd metal atom (*−*) site pairs (CH$_4$ + * + * → CH$_3$* + H*) on Pd (111) surfaces. Blue: Pd atom, gray: C atom, white: H atom. Bond distances are given in nanometer.

at 873 K; Table 1). We conclude that C−H bond activation limits rates on both O*-saturated Pd^0 and PdO cluster surfaces.

CH$_4$−O$_2$ reaction rates are independent of O$_2$ pressure before and after Pd−PdO transitions, indicating that the density of active sites and their reactivity on either O*-saturated Pd^0 or PdO cluster surfaces do not vary with reactant pressures. The marked increase in C−H activation rates upon Pd−PdO transitions reflects significant differences in the identity and reactivity of active sites for C−H bond activation on these two surfaces. First-order rate coefficients $[r_{\text{CH}_4}(\text{CH}_4)^{-1}]$ on O*-saturated Pd^0 and on PdO clusters are accurately described by eqs 1a and 1b, which differ only in their respective values for C−H activation rate constants ($k_{\text{C-H,O*/Pd}}$ and $k_{\text{C-H,PdO}}$, subscripts O*/Pd and PdO denote O*-saturated Pd^0 and PdO clusters, respectively):

$$\left.\frac{r_{\text{CH}_4}}{(\text{CH}_4)}\right|_{\text{O*/Pd}} = k_{\text{C-H,O*/Pd}}(\text{O}_2)^0 \tag{1a}$$

$$\left.\frac{r_{\text{CH}_4}}{(\text{CH}_4)}\right|_{\text{PdO}} = k_{\text{C-H,PdO}}(\text{O}_2)^0 \tag{1b}$$

C−H activation rate coefficients are ∼25-fold larger on PdO than on O* saturated Pd^0 surfaces at 873 K [12.9 vs 0.53 mol CH$_4$ (g-atom Pd$_{\text{surface}}$-kPa-s)$^{-1}$ on Pd clusters of 21.3 nm mean diameter, $k_{\text{C-H,PdO}}(k_{\text{C-H,O*/Pd}})^{-1}$ = 24.3, 873 K, Figure 3]. C−H bond activation rate coefficients are also larger on PdO than on uncovered Pd^0 clusters ($k_{\text{C-H,Pd}}$) during CO$_2$ or H$_2$O reactions with CH$_4$ [4.0 and 4.3 mol CH$_4$ (g-atom Pd$_{\text{surface}}$-kPa-s)$^{-1}$ on 12.5 nm mean Pd cluster diameter; thus $k_{\text{C-H,PdO}}(k_{\text{C-H,Pd}})^{-1}$ = 3.0−3.2, 873 K], on which C−H bonds in CH$_4$ are activated on site pairs of Pd metal atoms (*−*).[32]

In Sections 3.2 and 3.3, we probe mechanistic basis for these marked differences in rates (Figures 3 and 4) and in the barriers for the activation of the first C−H bond, the sole kinetically relevant step, on all surfaces examined. Barriers and reaction energies for the subsequent C−H activation steps have been previously reported on close-packed surfaces of Pd(111),[33] Co(0001),[33] Ru(0001),[34] Ni(111),[33] Rh(111),[33] and Pt(111)[33] and found to be much smaller than for the activation of the first C−H bond, except for the cleavage of the last C−H bond on metal sites. This latter step proceeds via an alternate route,

involving O* addition to form formyl intermediates that undergo C−H cleavage resulting in the formation of chemisorbed CO. The reactivity of PdO(101) and PdO(100) surfaces and the involvement of their lattice oxygens (O$_{\text{ox}}$) in the sequential oxidation of CH$_x$ intermediates will be reported in a later study. Here, we probe the structures and energies of adsorbed reactants, transition states, and products during the initial C−H bond activation of CH$_4$ on uncovered Pd(111), O*-saturated Pd(111), PdO(101), and PdO(100) surfaces as well as on uncovered and O*-saturated Pd clusters with 201 Pd atoms (Pd$_{201}$) and on PdO clusters with 94 Pd and 89 O atoms (Pd$_{94}$O$_{89}$).

3.2. Mechanistic Interpretations and Theoretical Treatments of C−H bond Activation over *−*, *−O*, and O*−O* Site Pairs on Pd(111) Surfaces and on a Cuboctahedral Pd Cluster with 201 Pd Atoms. Figure 5 shows the structures of reactant (**5a**), transition (**5b**), and product (**5c**) states for the first C−H bond activation in CH$_4$ on the uncovered Pd(111) surface. This step involves weakly adsorbed CH$_4$, which consists of an η_1-complex that forms via electron donation from a C−H bond to a Pd surface atom (Pd atom labeled "Pd$_1$" in Figure 5). Next, the C−H bond lengthens in a process that occurs concurrently with electron backdonation from Pd to the C−H antibonding ($\sigma^*_{\text{C-H}}$) orbital and with the incipient insertion of the Pd atom into the C−H bond to form the three center (H$_3$C···Pd···H)‡ transition state (**5b**); the latter ultimately decomposes into the CH$_3$−Pd and H−Pd products (**5c**) of this elementary step. This process closely resembles oxidative addition reactions of alkanes on mononuclear metal centers in organometallic complexes,[35] except that the back-donated electrons from the Pd surface are delocalized over the other metal atoms. As a result of electron delocalization, this step does not lead to full changes in valence for any specific Pd atom (e.g., the Pd atom labeled "1" in Figure 5) involved in the transition state. In contrast, changes in valence are required for similar reactions at metal centers in mononuclear organometallic complexes.[36,37]

On Pd(111) surfaces, the C−H bond length increases from 0.109 nm in CH$_4$(g) to 0.155 nm at the transition state. This process decreases the energy of $\sigma_{\text{C-H}}*$ antibonding states and thus allows for the backdonation of electrons from the metal into this state and the formation of strong Pd−C and Pd−H bonds at the transition state. The interaction of the C−H bond
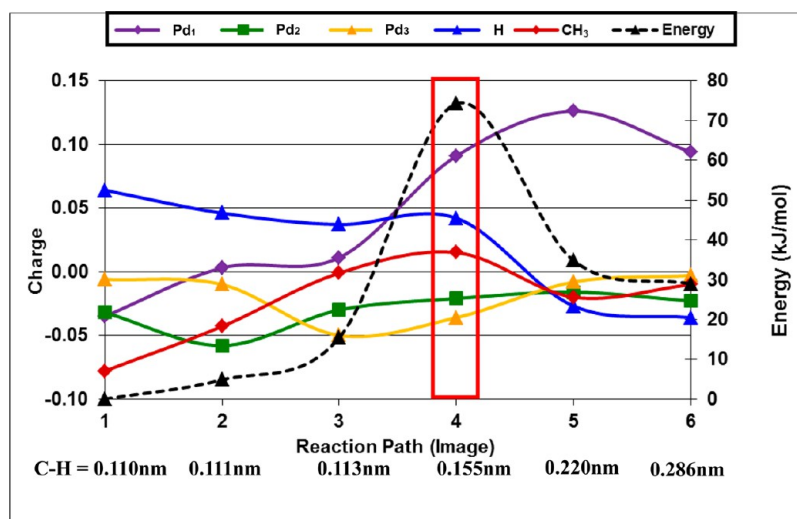
Figure 6. Change in Bader charges on Pd_1 (purple diamonds), Pd_2 (green squares), and Pd_3 (orange triangles) atoms in the Pd(111) surface and on dissociated H (blue triangles) and CH_3 (maroon diamonds) species and the reaction energy (black triangles) along the reaction coordinate during the C−H bond activation of methane over Pd(111) surfaces. The reaction coordinate is reported by the NEB images and the C−H bond distance between the reactant (image 1), transition state (highest energy, image 4), and product (image 6). Pd_1, Pd_2, and Pd_3 atoms are labeled in Figure 5.

with Pd leads to the formation of a three-centered $(H_3C\cdots Pd\cdots H)^{\ddagger}$ transition state (**5b**, Figure 5) with Pd−C and Pd−H bond distances for the Pd atom labeled Pd_1 of 0.219 nm (vs 0.206 nm in the product, **5c**) and 0.169 nm (vs 0.246 nm in the product, **5c**), respectively, and an activation barrier of 73 kJ mol^{-1}. The calculated transition-state structure (**5b**) and the activation barrier (73 kJ mol^{-1}) for C−H bond activation in methane on Pd(111) surfaces are very similar to those on the (111) surface of a Pd_{201} cluster (68 kJ mol^{-1}). These transition states resemble the products and contain nearly cleaved C−H bonds and therefore occur late along the reaction coordinate, allowing their stabilization by the Pd−C and Pd−H bonds formed in the final state. Similar transition-state structures have been reported for CH_4 activation on Pt(111),[31] Rh(111),[38] Ir(111),[39] and also on other 3d, 4d, and 5d transition metals.[40] These structures are also consistent with transition states proposed for CH_4 activation on mononuclear organometallic complexes [Pd-$(PH_3)_2$][41] and for C−H bond activation reactions of larger alkyl homologues on Pd(111),[42] which also proceed via oxidative addition processes.

Estimates of the charges on Pd atoms and the CH_3 and H fragments along the reaction coordinate as CH_4 evolves the $(H_3C\cdots Pd\cdots H)^{\ddagger}$ transition-state structures on Pd(111) surfaces (**5b**, Figure 5) are shown in Figure 6. These charge values along the reaction coordinate confirm that C−H bond activation proceeds via oxidative addition with electron donation from CH_4 to the metal surface and concurrent backdonation of electron density into the antibonding σ_{C-H}^* orbital of the activated C−H bond. These coupled electron-transfer steps cause only slight changes in charge (<0.1 e$^-$) along the reaction coordinate for all species involved (Pd atoms, CH_3 and H fragments). The charges on the Pd active center (atom Pd_1 in Figures 5 and 6) and the CH_3 fragment become slightly more positive (by +0.126 and +0.093 on Pd_1 and CH_3, respectively) and the H atom becomes slightly more negative (by −0.022) in moving from the reactant to the transition state. As in oxidative addition on organometallic clusters, the active metal center (Pd_1 in Figure 5) acts as both electrophile and nucleophile and, in doing so, shuttles electron density via concerted donation

from CH_4 to Pd and backdonation from Pd to σ_{C-H}^* antibonding states.[36,37]

As the oxygen chemical potentials increase, O* coverages increase and Pd atom-oxygen (*−O*) site pairs may form and activate C−H bonds via a different mechanism than on *−* sites, as also shown on Pt clusters [experimental: CH_4,[10] C_2H_6;[11] DFT: CH_4 on Pt_{201} clusters[10]]. In contrast with Pt, rate coefficients on Pd (Figure 3) do not show an intermediate kinetic regime, in which such site pairs become the prevalent C−H activation sites. These differences reflect stronger bonds with O* at Pd than Pt surfaces (DFT-calculated O* adsorption energies: −382 and −354 kJ mol^{-1} for Pd(111) and Pt(111) surfaces, respectively).[43] *−O* site pairs may become prevalent at higher temperatures and lower O_2 pressures than in the current study, as O* species are removed via recombinative desorption or faster reactions with CH_4 to expose Pd centers. These Pd atom-oxygen (*−O*) site pairs were examined using theory to probe the influence of O* binding energies on C−H bond activation barriers. Reactant, transition state, and product structures and activation and reaction energies were calculated on Pd(111) at 0.11−0.67 ML O*-coverages (details in Supporting Information, Section 2). At 0.67 ML O*, the C−H activation barrier (117 kJ mol^{-1}) is significantly higher than on bare Pd(111) (73 kJ mol^{-1}). On *−O* site pairs, C−H activation proceeds via Pd atom insertion into the C−H bond and concerted H-abstraction by vicinal O* species. C−H bonds at the transition state on 2/3 ML O* covered Pd(111) surfaces (0.136 nm, Figure S2a, structure (**S2a.ii**)) are shorter than on bare Pd(111) surfaces (0.155 nm, (**5b**)), an indication that the transition state (**S2a.ii**) occurs earlier along the reaction coordinate. O* causes some repulsion with CH_3* groups at the transition state, thus weakening Pd$\cdots$CH$_3$ and Pd$\cdots$H bonds, which are longer (by 0.013 and 0.045 nm, respectively) than for the transition state on bare Pd(111) surfaces (**5b**). These repulsive interactions lead to higher activation barriers on *−O* sites (at 2/3 ML O*; 117 kJ mol^{-1}) than on bare Pd(111) surfaces (*−*; 73 kJ mol^{-1}). These barriers become even higher as O* coverages decrease (117 and 133 kJ mol^{-1} for 0.67 and 0.13 ML O*; Figure S2b) because O* species become more strongly bound and less reactive. Thus, we
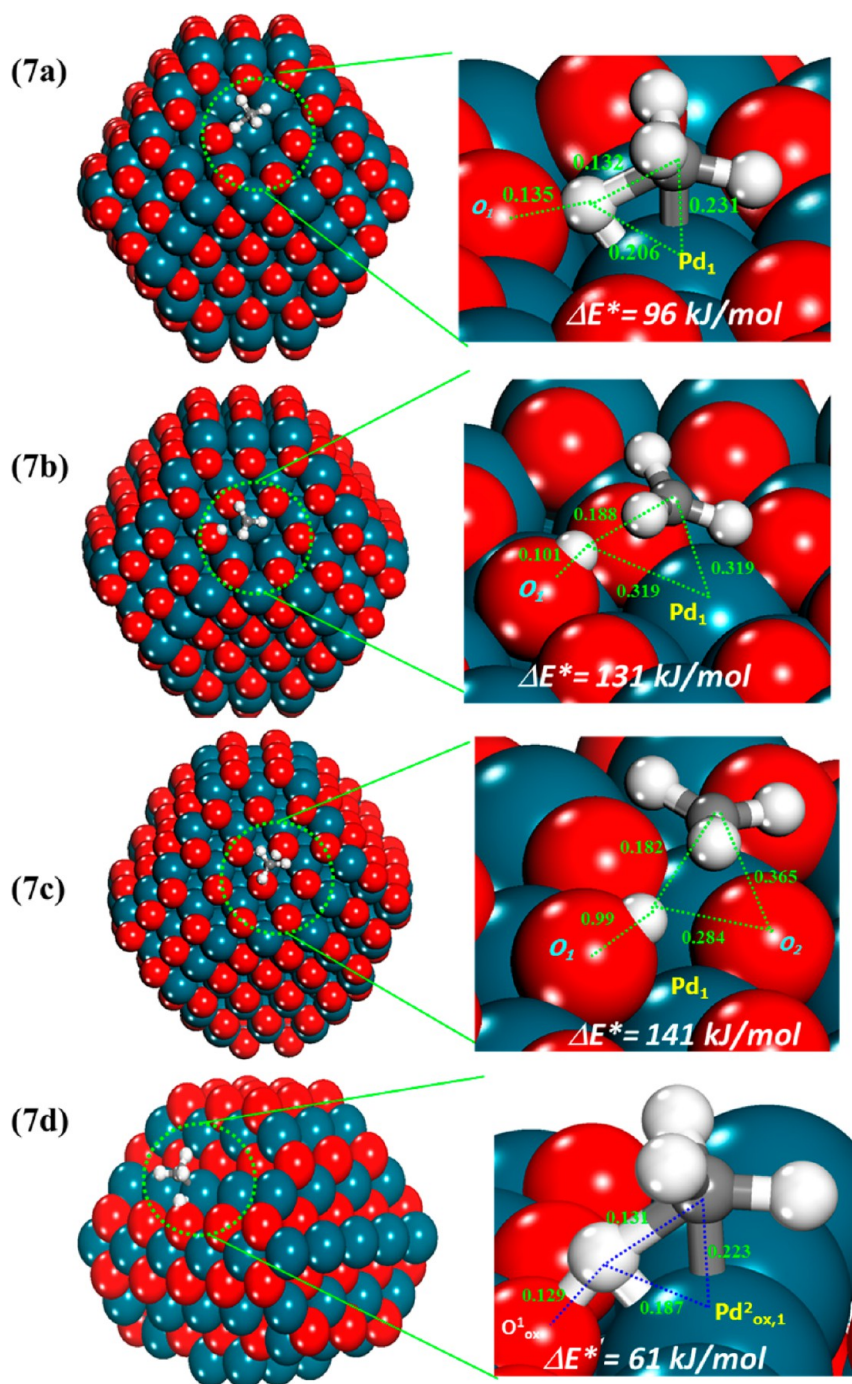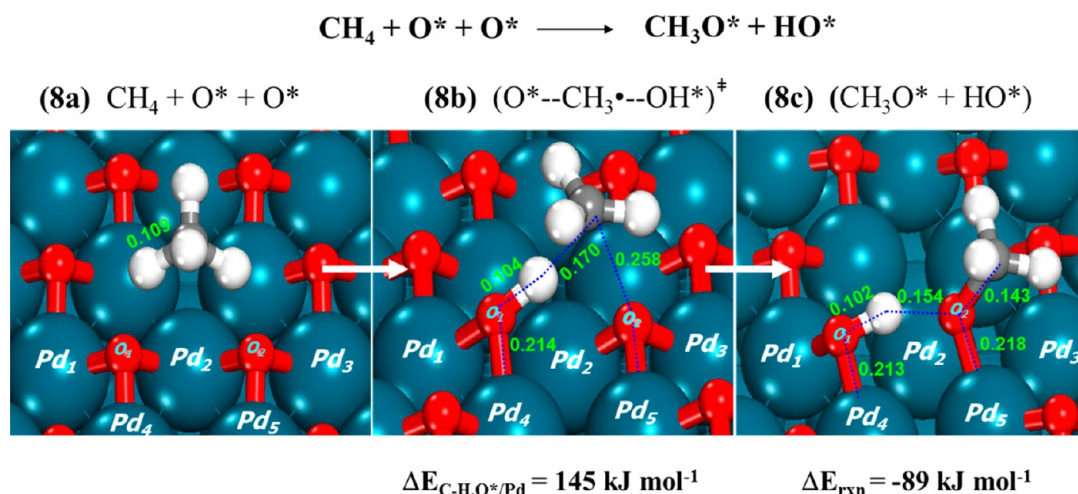
Figure 7. DFT-calculated transition-state structures and activation energies (in kJ mol^{-1}; with respect to the energy of gas phase CH$_4$) for C−H bond activation steps on **(7a)** Pd metal−oxygen (*−O*) site pairs (labeled Pd$_1$−O$_1$) (CH$_4$ + * + O* → CH$_3$* + OH*) on the (111) surface of cuboctahedral Pd clusters with 201 Pd atoms covered with 0.985 ML of O* atoms (three oxygen vacancy sites); **(7b)** Pd metal−oxygen (*−O*) site pairs (labeled Pd$_1$−O$_1$) (CH$_4$ + * + O* → CH$_3$* + OH*) on the (111) surface of cuboctahedral Pd clusters with 201 Pd atoms covered with 0.995 ML of O* atoms (one oxygen vacancy sites); **(7c)** oxygen atom (O*−O*) site pairs (labeled O$_1$−O$_2$) (CH$_4$ + O* + O* → CH$_3$O* + OH*) on the (111) surface of cuboctahedral Pd clusters with 201 Pd atoms covered with 1 ML of O* atoms; and **(7d)** Pd$_{ox}$−O$_{ox}$ site-pair (labeled Pd$^2_{ox,1}$−O$^1_{ox}$) (CH$_4$ + Pd$_{ox}$ + O$_{ox}$ → CH$_3$Pd$_{ox}$ + O$_{ox}$H) on the PdO(101) facet of 183 atom PdO (Pd$_{94}$O$_{89}$) clusters. Bond distances are given in nanometer.

conclude that *−O* site pairs are less effective than *−* site pairs for C−H bond activation on Pd surfaces.

The structures and energies of C−H activation transition states were also calculated on *−O* site pairs at (111) surfaces of Pd$_{201}$ clusters nearly saturated with O* and containing either one oxygen vacancy (0.995 ML) or three oxygen vacancies (0.985 ML). These clusters expand outward to allow for O* coverages of 1 ML (Section 2.3), thus providing a more

accurate representation of the sites and coverages found in practice than Pd(111) surfaces. Transition state structures at one and three oxygen vacancy sites on Pd$_{201}$ clusters are shown in Figure 7, as structures **(7b)** and **(7a)**, respectively. The activation barrier on one-vacancy *−O* sites at Pd$_{201}$ cluster surfaces (Figure 7, **(7b)**) was slightly higher (by ∼14 kJ mol^{-1}) than on *−O* sites on 2/3 ML O*/Pd(111) surfaces (Figure S2a, **(S2a.ii)**), because of slightly stronger repulsion between

$$CH_4 + O* + O* \longrightarrow CH_3O* + HO*$$

(8a) $CH_4 + O* + O*$ **(8b)** $(O*\text{--}CH_3{}^\bullet\text{--}OH*)^\ddagger$ **(8c)** $(CH_3O* + HO*)$

$$\Delta E_{C\text{-}H,O*/Pd} = 145 \text{ kJ mol}^{-1} \qquad \Delta E_{rxn} = -89 \text{ kJ mol}^{-1}$$

Figure 8. DFT-calculated structures of reactant (**8a**), transition (**8b**), and product (**8c**) states and energy changes (in kJ mol^{-1}) for C−H bond activation steps over O*−O* site pairs (labeled O_1−O_2) ($CH_4 + O* + O* \rightarrow CH_3O* + OH*$) on 0.67 ML O*-covered Pd (111) surfaces. Blue: Pd atom, red: O atom, gray: C atom, white: H atom. Bond distances are given in nanometer.
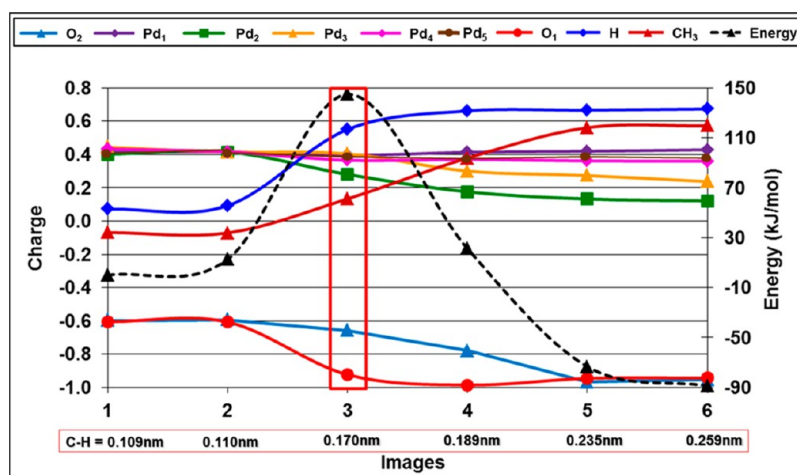

Figure 9. The change in Bader charges on Pd_1 (purple diamonds), Pd_2 (green squares), Pd_3 (orange triangles), Pd_4 (magenta diamonds), and Pd_5 (brown circles) atoms in the 0.67 ML O* covered Pd(111) surface, dissociated H (blue diamonds) and CH_3 (maroon triangles) species, active O_1 (red circles) and O_2 (blue triangles) species that result in OH* and CH_3O*, respectively, and the reaction energy (black triangles) along the reaction coordinate during the C−H bond activation of methane over the O*−O* site pair on the 0.67 ML O* covered Pd(111) surface. The reaction coordinate is reported by the NEB images and the C−H bond distance between the reactant (image 1), transition state (highest energy, image 3), and product (image 6). Pd_1, Pd_2, Pd_3, Pd_4, Pd_5, O_1, and O_2 are labeled in Figure 8.

O* and CH_3 groups at the higher coverages on Pd cluster surfaces. Activation barriers on O*-covered Pd_{201} clusters decrease from 131 to 96 kJ mol^{-1} as two additional vacancies become available (Figure 7, (**7a**)). The three-vacancy sites form a larger Pd ensemble that allows the CH_3 fragment access to Pd centers without repulsion by vicinal O*, a conclusion confirmed by the shorter and stronger Pd···CH_3 bonds (0.231 nm, (**7a**)) than on the single-vacancy structure (0.319 nm, (**7b**)).

O*-saturated surfaces lack oxygen vacancies and exposed Pd atoms (*), thus requiring C−H bond activation to occur on O*−O* site pairs, as shown in Figure 8 on O*-covered Pd(111) surfaces and Figure 7c on O* saturated Pd_{201} clusters. This step involves H-abstraction from CH_4 by an O* (O_1 in Figure 8b) in the O*−O* pair to form a loosely bound CH_3 fragment and a nearly formed O−H* bond (0.104 vs 0.102 nm in the product state) as well as an essentially cleaved C−H bond [0.170 vs 0.109 nm in $CH_4(g)$] at the (O*··· $CH_3{}^\bullet$···*OH)‡ transition state (**8b**). This homolytic C−H

bond activation to form $CH_3{}^\bullet$ occurs via electron transfer from H$^\bullet$ to O* during the H-abstraction process. The $CH_3{}^\bullet$ group interacts weakly (−6 kJ mol^{-1}) with the vicinal O* (labeled as O_2 in (**8b**)) at the transition state and its long O*···CH_3 distance (0.258 nm) relative to that in the bound methoxy products (0.143 nm; **8c**), taken together with its sp$_2$ configuration, confirm its radical-like character. Weak interactions with O* (labeled as O_2 in (**8b**)) or H−O* preclude $CH_3{}^\bullet$ stabilization at the transition state, in contrast with the strong Pd−CH_3 bonds at C−H activation transition states on uncovered surfaces (**5b**); as a result, activation barriers are much larger on O*−O* site pairs (145 kJ mol^{-1}) than *−* site pairs (73 kJ mol^{-1}). The transition-state structures for the activation of methane on O*−O* sites at 0.67 ML O*-covered Pd(111) surfaces [(**8b**), in Figure 8b] are nearly identical to those on 1 ML O*-covered Pd_{201} clusters [(**7c**), in Figure 7c]. The activation barriers were within 4 kJ mol^{-1} for the two structures (145 and 141 kJ mol^{-1} for the cases of 2/3 ML O*-
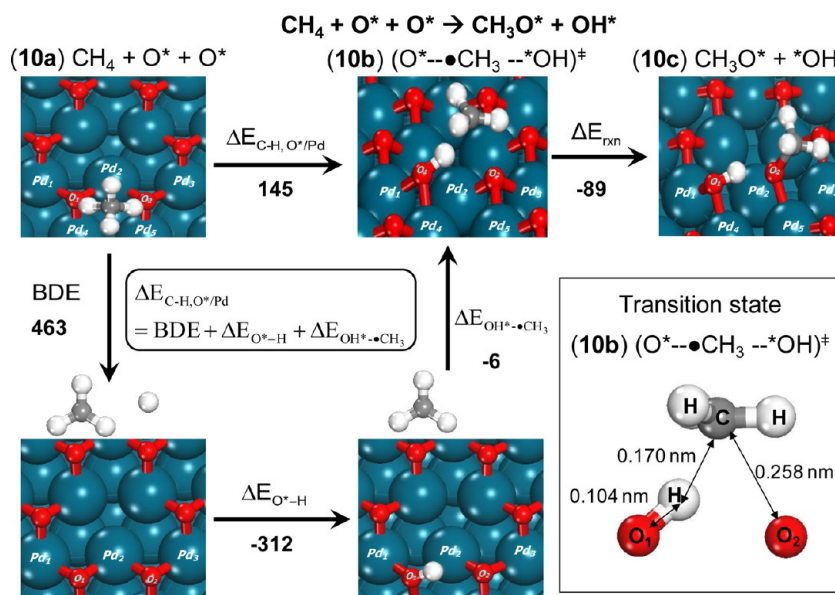
Figure 10. Born−Haber thermochemical cycle analysis (eq 2) of the activation enthalpies ($\Delta E_{C-H, O*/Pd}$) for C−H bond activation steps over O*−O* site pairs (labeled O_1−O_2) ($CH_4 + O* + O* \rightarrow CH_3O* + OH*$) on 0.67 ML O* covered Pd (111) surfaces. Blue: Pd atom, red: O atom, gray: C atom, white: H atom. Enthalpy values are given in kJ mol^{-1}.

Table 2. DFT-Calculated Interaction Energies of C−H Bond Activation Transition-State Complexes and Adsorption Energies of H Radicals on Chemisorbed or Lattice Oxygen Atoms at O*/Pd(111), PdO(101), and PdO(100) Surfaces

	interaction energy $\Delta E_{O*-H}{}^{a,b}$ (kJ mol^{-1})	interaction energy $\Delta E_{OH*-{}^{\bullet}CH_3}{}^{c,b}$ (kJ mol^{-1})	interaction energy $\Delta E_{CH_3-O*/Pd}{}^{d,b}$ (kJ mol^{-1})	adsorption energy $\Delta E_{OH*-O*}{}^{e}$ (kJ mol^{-1})
O*/Pd(111)	−312	−6	+22	−321
	interaction energy $\Delta E_{O_{ox}-H}{}^{f,b}$ (kJ mol^{-1})	interaction energy $\Delta E_{Pd_{ox}-CH_3}{}^{g,b}$ (kJ mol^{-1})	interaction energy $\Delta E_{CH_3-PdO}{}^{d,b}$ (kJ mol^{-1})	adsorption energy $\Delta E_{O_{ox}H-O_{ox}}{}^{h}$ (kJ mol^{-1})
PdO(101)	−164	−238	−125	−299
PdO(100)	−198	−135	−92	−

[a]Interaction energy between gas-phase H radicals and O* atoms. [b]In the transition-state geometries. [c]Interaction energy between the CH$_3$ fragments and surfaces (including the H leaving group bound to the vicinal O*); [d]Interaction energy between the CH$_3$ fragments and the surfaces (with H from the cleaved C−H bond removed from the surfaces); [e]Difference in OH* and O* adsorption energies. [f]Interaction energy between gas-phase H radicals and O$_{ox}$ atoms. [g]Interaction energy between the CH$_3$ fragments and surfaces (including the H leaving group binds to the vicinal O$_{ox}$). [h]Difference in O$_{ox}$H and O$_{ox}$ adsorption energies.

covered Pd(111) surface and 1 ML O*-saturated Pd$_{201}$ cluster, respectively, Table 1).

Figure 9 shows the charges in CH$_3$, H, O (oxygen atoms O$_1$ and O$_2$, labeled in Figure 8), and Pd (Pd atoms Pd$_i$, i = 1−5, labeled in Figure 8) species along the reaction coordinate for C−H bond activation on O*−O* site pairs. This C−H bond activation step proceeds via H-abstraction of methane by O* (labeled O$_1$ in Figure 8) and concerted electron transfer from the H atom leaving group to the O*, through a late transition state lacking one C−H bond in the CH$_4$ reactant (0.170 nm bond length, structure (8b)). The charge at the H-atom increases from +0.071 in reactants to +0.550 at the (O*⋯CH$_3{}^{\bullet}$⋯*OH)‡ transition state, while that at O$_1$ (as labeled in Figure 8) becomes more negative (−0.605 to −0.923). The electron transfer occurs just before the transition state, as shown by charges on the leaving H (+0.550) and O$_1$ (−0.923, atom O$_1$ in Figure 8) atoms at the transition state, which are more similar to those in OH* products (+0.673 and −0.943 for H and O$_1$, respectively, image 6 of Figure 9) than in the H and O$_1$ atoms in the reactant state (+0.071 and −0.605 for H and O$_1$, respectively, image 1 of Figure 9). The CH$_3{}^{\bullet}$ species are essentially uncharged at the transition state (+0.133) but become cationic (+0.572) in the *OCH$_3$ products. The charge

transferred from H$^{\bullet}$ to O* (O$_1$ in Figure 8) is localized at the vicinal Pd$_2$ and Pd$_4$ centers (in Figure 8), whose valences decrease from +0.401 and +0.432 in the reactant state (image 1, Figure 9) to +0.280 and +0.365, respectively, at the transition state (image 3, Figure 9). The charge transfer from CH$_3{}^{\bullet}$ to the vicinal O* (O$_2$ in Figure 8) does not occur until very late along the reaction coordinate and is localized on the Pd$_3$ and Pd$_5$ (as shown in Figure 8) whose valences decrease from +0.443 and +0.420 in the reactant state to +0.237 and +0.396 in the product state, respectively. Such C−H activation paths and the radical-like alkyl fragments (8b) at their transition states have been proposed for C−H bond activation of CH$_4$ on O* saturated Pt(111) surfaces and cuboctahedral 201-atom Pt clusters[10] and for C−H activation of larger alkanes on reducible oxides (VO$_x$).[44,45]

C−H activation barriers on O*−O* pairs ($\Delta E_{C-H,O*/Pd}$) can be dissected into energies for a sequence of hypothetical steps using Born−Haber thermochemical cycles (Figure 10; Table 2), which exploit the path-independence of thermodynamic state functions. These steps include homolytic C−H bond cleavage of gaseous CH$_4$ (BDE) as well as reactions of O* (labeled O$_1$ in Figure 8) with gaseous H-radicals (ΔE_{O*-H}) and of a vicinal O* (labeled O$_2$ in Figure 8) with a CH$_3{}^{\bullet}$ radical

$$CH_4 + Pd_{ox} + O_{ox} \longrightarrow CH_3Pd_{ox} + O_{ox}H$$
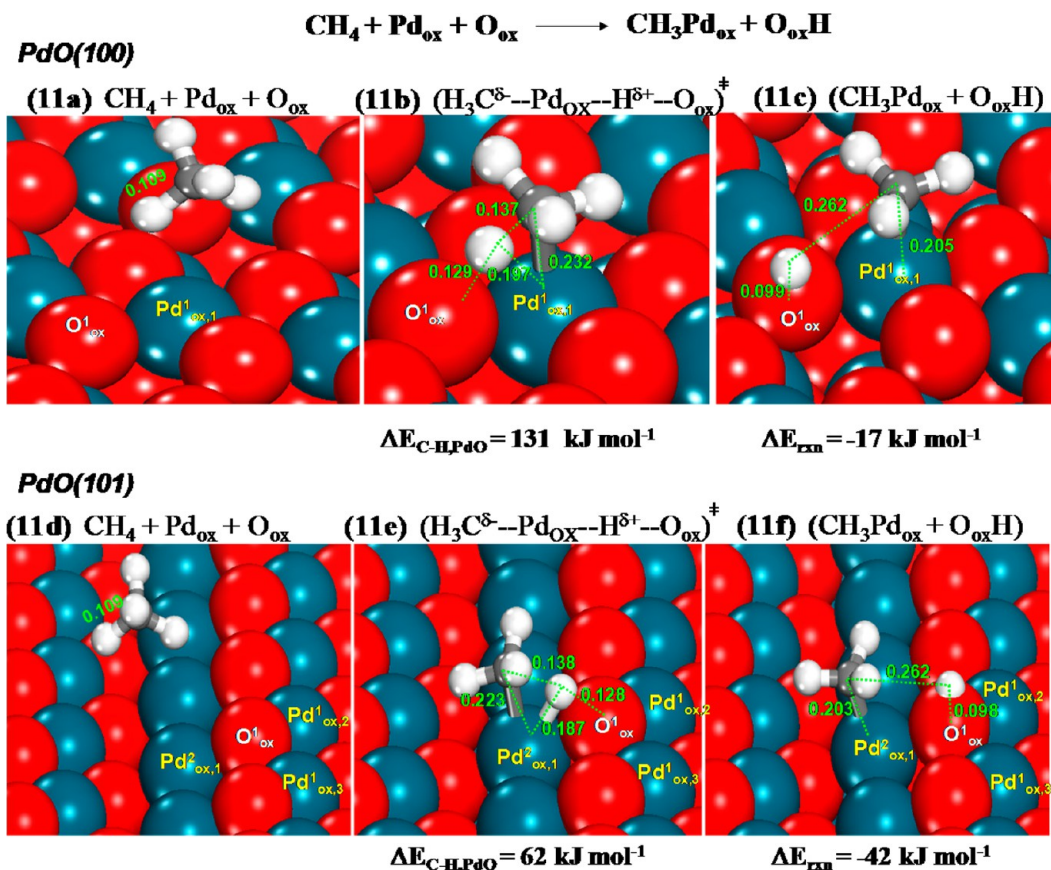
Figure 11. DFT calculated structures of reactant (**11a**), transition (**11b**), and product (**11c**) states and energy changes (kJ mol^{-1}) for C−H bond activation steps on nonstoichiometric Pd_{ox}−O_{ox} site pairs (labeled $Pd^1_{ox,1}$−O^1_{ox}) ($CH_4 + Pd_{ox} + O_{ox} \rightarrow CH_3Pd_{ox} + O_{ox}H$) at PdO (100) surfaces. Similarly, the calculated energies and optimized reactant (**11d**), transition (**11e**), and product (**11f**) states for C−H bond activation steps on stoichiometric Pd_{ox}−O_{ox} site pairs (labeled $Pd^2_{ox,1}$−O^1_{ox}) at the PdO(101) surface are shown in (**11d**), (**11e**), and (**11f**), respectively. Blue: Pd atom, red: O atom, gray: C atom, white: H atom. Bond distances are given in nanometer.

($\Delta E_{OH*-\cdot CH_3}$), leading to an activation barrier ($\Delta E_{C-H,O*/Pd}$) given by the sum of their respective reaction energies:

$$\Delta E_{C-H,O*/Pd} = BDE + \Delta E_{O*-H} + \Delta E_{OH*-\bullet CH_3} \quad (2)$$

$CH_3^\bullet$ interactions with O*-covered surfaces are weak at the transition state ($\Delta E_{OH*-\cdot CH_3} = -6$ kJ mol^{-1}) and $CH_3^\bullet$ species remain distant from O* (labeled O_2 in structure (**8b**) of Figure 8, $H_3C^\bullet \cdots O^*$ distance of 0.258 nm). Thus, activation barriers are sensitive only to interactions between H-radicals (the leaving group) and O* atoms ($\Delta E_{O*-H} = -312$ kJ mol^{-1}), which is similar to the OH* formation energies, defined as the difference between the energy of OH* products and the combined energy of the O* and gaseous $H^\bullet$ (at noninteracting distances, $\Delta E_{OH*-O*} = -321$ kJ mol^{-1}, Table 2) and equaled the difference in the heats of OH* and O* adsorption and also the oxygen basicity. The similar values of ΔE_{O*-H} (at transition states; −312 kJ mol^{-1}) and ΔE_{OH*-O*} (in product configurations; −321 kJ mol^{-1}) reflect the nearly fully formed $O \cdots H^*$ bonds at these transition states. The reaction proceeds via a H-abstraction by O* together with a concerted electron transfer from the hydrogen to the O* thus resulting in a nearly fully formed O−H bond in the transition state along with a weakly interacting CH$_3$ free radical-like intermediate. We conclude that C−H activation barriers depend sensitively on the basic character of the chemisorbed O*, found for the case on O*−O* pairs and similar to that found for metal atom-oxygen pairs,

as shown from the linear relation between the barriers and heats of atomic oxygen adsorption on Pt(111)[10] and Pd(111) (Supporting Information, Section 2, Figure S2c) surfaces. The trend of higher oxygen basicity, found in weakly adsorbed oxygen prevalent at high O* coverages, with lower barriers is ubiquitous for C−H bond activation[10,31] and consistent with previous findings of oxygen atoms acting as Brønsted bases in the dissociation of acidic C−H bonds[46] [in $(CH_3)_2CO$].[47]

3.3. Mechanistic Interpretations and Theoretical Treatments of C−H Bond Activation Steps on Pd_{ox}−O_{ox} Site Pairs at PdO Surfaces and PdO ($Pd_{94}O_{89}$) Clusters. Here, we first examine C−H activation steps on extended PdO(100) and PdO(101) surfaces and then on PdO ($Pd_{94}O_{89}$) clusters. The C−H activation transition states are stabilized on these structures by four-center interactions between the Pd^{2+}, $CH_3^{\delta-}$, $H^{\delta+}$, and O^{2-}. The four-center concerted nature of these interactions ($H^{\delta+}$ with O^{2-}, O^{2-} with Pd^{2+}, Pd^{2+} with $CH_3^{\delta-}$, and $CH_3^{\delta-}$ with $H^{\delta+}$) leads to activation barriers much smaller than on O*−O* pairs and to the sharp increase in CH_4−O_2 reaction rates observed as Pd−PdO phase transitions occur.

Clusters and extended surfaces of PdO predominantly expose low-energy PdO(100) and PdO(101) facets containing Pd^{2+} centers (Pd_{ox}) assembled in rows. On both surfaces, Pd centers lie between rows of O^{2-} atoms (O_{ox}) (Figure 1c,d, respectively) but with surface Pd:O stoichiometries of 1:2 on PdO(100) and 1:1 on PdO(101).[22] Exposed Pd_{ox} centers can interact with the

C-atom in CH_4, even without the presence of O-vacancies, on both surfaces, while H-atoms are abstracted by vicinal O_{ox} atoms. CH_3 interactions with Pd centers are, however, not possible on O*-saturated Pd surfaces, because of their dense and impervious O* adlayer (Section 3.2), which are absent on the corrugated surfaces of PdO(100) and PdO(101).

C−H bond activation barriers were calculated over the nonstoichiometric $Pd^1_{ox,1}$−O^1_{ox} site pairs on the PdO(100) surface (in Figure 1c) and stoichiometric $Pd^2_{ox,1}$−O^1_{ox} site pairs on the PdO(101) surface (in Figure 1d). As discussed in Section 2.3, the O^2_{ox} centers that are also present on PdO(101) are inaccessible as they coordinate to 4 Pd centers as shown in Figure 1d. As such, the $Pd^1_{ox,1}$−O^2_{ox} and $Pd^2_{ox,1}$−O^2_{ox} site pairs on the PdO(101) surface were not examined. The $Pd^1_{ox,1}$−O^1_{ox} sites on the PdO(101) surface were also not examined as they are identical to those on PdO(100). The optimized structures of the reactant, transition, and product states on non-stoichiometric $Pd^1_{ox,1}$−O^1_{ox} site pairs on PdO(100) are shown in Figures 11a−c. The transition state (11b) is remarkably similar to that for C−H activation on Pd atom-oxygen (*−O*) site pairs on O*-covered Pd(111) surfaces (S2a.ii) (Section 3.2) with C−H, O−H, and Pd−C bond distances that differ by <0.002 nm for the two transition-state structures. The Pd−H bond at the transition state is, however, shorter on PdO(100) (0.197 nm) than on *−O* sites on Pd(111) (0.214 nm), consistent with the more effective stabilization of the H-atom at PdO(100) surfaces. In spite of the similar geometries and bond distances between the two transition states [(11b) and (S2a.ii)], the C−H activation barrier on PdO(100) (131 kJ mol^{-1}) is higher than that on *−O* sites at Pd(111) surfaces with 0.67 ML O* (117 kJ mol^{-1}). The difference is caused by electronic differences between the O*-covered metals and metal oxides and by the concomitant differences in charge at the various atoms involved in each transition state.

PdO(100) surfaces are more stable than PdO(101) surfaces, but they are less active for C−H bond activation.[48] The DFT-derived C−H bond activation barriers on the nonstoichiometric $Pd^1_{ox,1}$−O^1_{ox} site pairs on PdO(100) are about 2-fold higher than on stoichiometric $Pd^2_{ox,1}$−O^1_{ox} sites on PdO(101) (131 vs 62 kJ mol^{-1}), consistent with reported values [104,[49] 154,[50] and 118 kJ mol^{-1} [48] on PdO(100) and 64 kJ mol^{-1} [51] on PdO(101)]. The low activation barrier on PdO(101) calculated here (62 kJ mol^{-1}) is nearly identical to our measured barrier (61 kJ mol^{-1}) on PdO clusters (Table 1). The higher calculated barriers on PdO(100) reflect the weaker interaction between the Pd_{ox} centers ($Pd^1_{ox,1}$ in Figure 11a−c) and the CH_3 fragments in the transition state compared with that of Pd_{ox} ($Pd^2_{ox,1}$ in Figure 11d−f) at the transition state that mediate C−H activation on PdO(101) surfaces, a conclusion evident from the structures, energies, and charges of the transition state and along the reaction coordinate (Section 3.4)

We focus most of the detailed discussion herein on the more active PdO(101) surface (Figure 1d) but will return to the comparison of the PdO(100) and PdO(101) surfaces in Section 3.4. The structures of reactants, transition states, and products in C−H bond activation steps on Pd_{ox}−O_{ox} pairs ($Pd^2_{ox,1}$−O^1_{ox} in Figure 1d) over the PdO(101) surface are shown in Figure 11 (structures (11d−f), respectively). The active Pd_{ox} atoms ($Pd^2_{ox,1}$ in Figure 11d−f) exposed at PdO(101) surfaces oxidatively insert into a C−H bond of CH_4 while vicinal O_{ox} (O^1_{ox} in Figure 11d−f) species concurrently abstract the H atom to form four-center transition

states $(H_3C^{\delta-}···Pd_{ox}···H^{\delta+}···O_{ox})^{\ddagger}$ (11e), in pathways reminiscent of σ−bond metathesis[36,52,53] or oxidative hydrogen migration[54] in organometallic complexes, which are also mediated by four-center transition states. The stabilization of the $CH_3^{\delta-}$ and $H^{\delta+}$ fragments that form in the transition state leads to an activation barrier of 62 kJ mol^{-1}. The calculations for the C−H bond activation of CH_4 on the stoichiometric Pd_{ox}−O_{ox} sites (labeled $Pd^2_{ox,1}$−O^1_{ox} in Figure 7d) on the (101) surface of $Pd_{94}O_{89}$ clusters (Figure 2b) gave very similar transition-state structures ((7d), Figure 7d) and activation energies (61 kJ mol^{-1}) as on PdO(101) surfaces ((11e), Figure 11e; 62 kJ mol^{-1}). Alternate C−H activation routes assisted by O_{ox}−O_{ox} site-pairs (labeled O^1_{ox}−O^1_{ox} in Figure 1d) at PdO(101) surfaces require activation energies much higher than on Pd_{ox}−O_{ox} site-pair ($Pd^2_{ox,1}$−O^1_{ox} in Figure 11d−f) [196 vs 62 kJ mol^{-1}]; the values are even higher than those found on O*−O* pairs on O*-saturated Pd^0 surfaces (145 kJ mol^{-1}, Section 3.2). Consequently, O_{ox}−O_{ox} pairs are much less reactive than Pd_{ox}−O_{ox} pairs for C−H bond activation on PdO surfaces.

We conclude that C−H activation on the active PdO(101) surfaces involves Pd_{ox}−O_{ox} site pairs and proceeds via oxidative addition of coordinatively saturated Pd_{ox} ($Pd^2_{ox,1}$ in Figure 11d−f) into the C−H bond and simultaneous H-abstraction by vicinal O_{ox} (O^1_{ox} in Figure 11d−f) species. The $CH_3^{\delta-}$ fragment is stabilized by the Pd^{2+} center ($Pd^2_{ox,1}···CH_3$ bond distances are 0.223 nm at the transition state (11e) vs 0.203 nm in the product state, (11f), Figure 11) and also by residual bonding and Coulombic interactions with the $H^{\delta+}$ atom in CH_4 as the latter incipiently binds to O_{ox} (C−H bond distances are 0.138 nm at the transition state vs 0.109 nm in $CH_4(g)$). The $H^{\delta+}$ atom at the transition state (11e) is stabilized not only by $CH_3^{\delta-}$−$H^{\delta+}$ (0.138 nm) and Pd_{ox}−$H^{\delta+}$ (0.187 nm) interactions but also by the formation of strong O_{ox}−$H^{\delta+}$ bonds (0.128 vs 0.098 nm in OH products, Figure 11, structure (11f)). $H_3C···H$ bonds are shorter (0.138 vs 0.155 nm) and $Pd···CH_3$ and $Pd···H$ bonds are longer (0.223 vs 0.219 nm and 0.187 vs 0.169 nm, respectively) than in the transition state for CH_4 activation on Pd(111) surfaces ((5b), Figure 5), consistent with an earlier transition state on PdO(101) than on Pd(111) surfaces.

These conclusions are consistent with precedents from organometallic complexes ($Ir(PH_3)_2H$,[37] $W(OH)_2(=NH)$[55]), on which C−H bonds are activated via oxidative addition and σ-bond metathesis routes, respectively,[37,55] but in the latter case, organic ligands [e.g. NH in $W(OH)_2(=NH)$[55]] instead of O_{ox} atoms stabilize transition states. In oxidative addition routes, bond distances for C···H and M···CH_3 (M denotes metal) at transition states are similar on $Ir(PH_3)_2H$[37] and Pd(111) (C−H bond distances of 0.155 nm in both systems and M···CH_3 distances of 0.223 and 0.219 nm for $Ir(PH_3)_2H$ and Pd(111), respectively). M···H bond distances were also similar at 0.160 and 0.169 nm on $Ir(PH_3)_2H$[37] and Pd(111), respectively. For the σ-bond metathesis pathway, C···H and M···CH_3 bond distances on $W(OH)_2(=NH)$[55] complexes were found to be similar to those on PdO(101) surfaces (Figure 11, structure (11e)). C···H bonds were 0.147 nm on $W(OH)_2(=NH)$[55] and 0.138 nm on PdO(101) surfaces and M···CH_3 bonds were slightly shorter on $W(OH)_2(=NH)$ complexes (0.223 nm)[55] than on PdO(101) (0.236 nm). The M···H bond lengths are also similar for σ-bond metathesis transition states on $W(OH)_2(=NH)$ complexes[55] (0.186 nm) and on PdO (0.187 nm; (11e)) but shorter than at oxidative addition transition states, because H leaving groups in σ-bond

15437

dx.doi.org/10.1021/ja405004m | J. Am. Chem. Soc. 2013, 135, 15425−15442
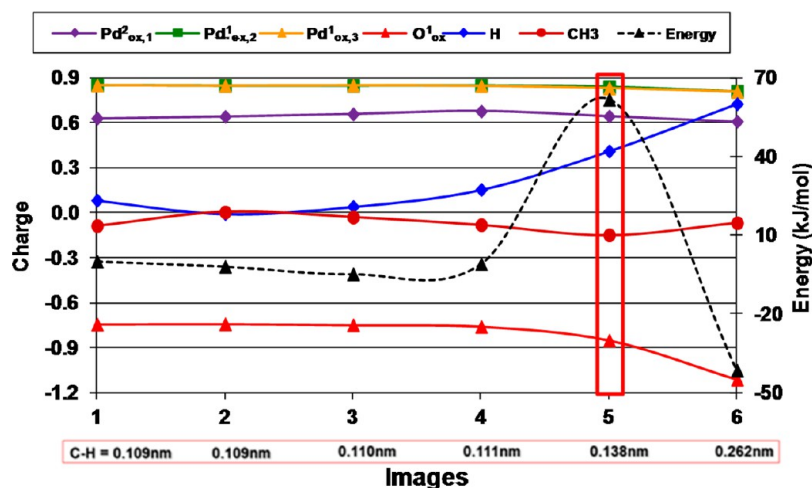
Figure 12. The change in Bader charges on $Pd^2_{ox,1}$ (purple diamonds), $Pd^1_{ox,2}$ (green squares), and $Pd^1_{ox,3}$ (orange triangles) atoms in the PdO(101) surface, dissociated H (blue diamonds), and CH_3 (maroon circles) fragments, active O^1_{ox} (red triangles) species, and the reaction energy (black triangles) along the reaction coordinate during C−H bond activation of methane over Pd_{ox}−O_{ox} site pair (labeled $Pd^2_{ox,1}$−O^1_{ox}) on the PdO(101) surface. The reaction coordinate is reported by the NEB images and the C−H bond distance between the reactant (image 1), transition state (highest energy, image 5), and product (image 6). The $Pd^2_{ox,1}$, $Pd^1_{ox,2}$, $Pd^1_{ox,3}$, O^1_{ox} sites are labeled in Figure 11d−f.
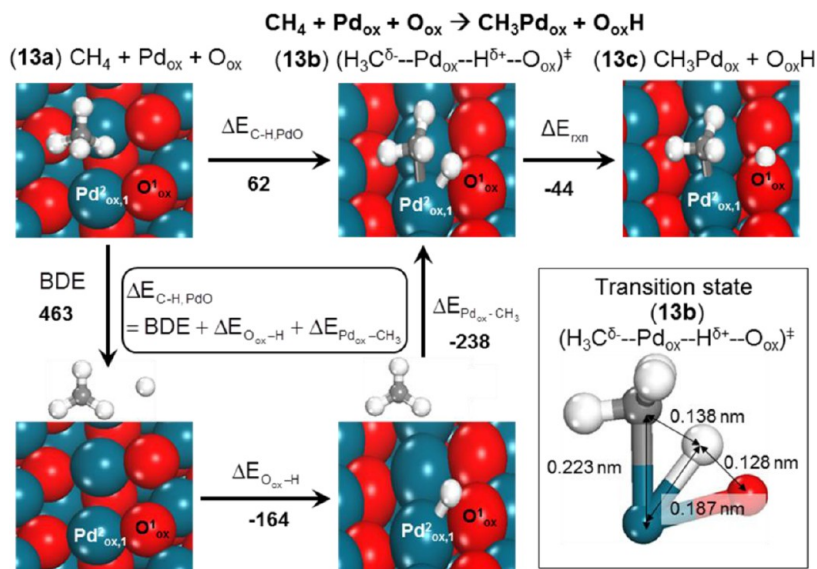
Figure 13. Born−Haber thermochemical cycle analysis (eq 3) constructed for the activation enthalpies ($\Delta E_{C-H,PdO}$) of C−H bond activation steps on Pd_{ox}−O_{ox} site pairs (labeled $Pd^2_{ox,1}$−O^1_{ox}) ($CH_4 + Pd_{ox} + O_{ox} \rightarrow CH_3Pd_{ox} + O_{ox}H$) at PdO (101) surfaces. Blue: Pd atom, red: O atom, gray: C atom, white: H atom. Enthalpy values are given in kJ mol^{-1}.

metathesis routes are stabilized by both metal centers and ligands (NH in W(OH)$_2$(=NH) and O_{ox} in PdO) and their transition states occur earlier along the reaction coordinate. These bond distances and transition-state structures clearly illustrate the mechanistic connections between C−H activation in organometallic complexes and in metal and oxide surfaces. On both systems, the metal atom acts as the sole nucleophile and electrophile and as the ultimate binding site for both the CH_3 and H fragments during oxidative addition. For the case of the metal−ligand pair (Pd$_{ox}$−O_{ox} on PdO, Pd−oxygen (*−O*) on O* covered Pd^0 surfaces, W and NH in W(OH)$_2$(=NH)[55]), the metal acts as the nucleophile and the metal−ligand pair as the electrophile and the ultimate binding sites for the CH_3 and H fragments during σ-bond metathesis.

Figure 12 shows the evolution of charges in Pd$_{ox}$ and O_{ox} sites and in CH_3 and H fragments along the reaction

coordinate. C−H dissociation proceeds via electron donation from the C-atom in CH_4 to the Pd$_{ox}$ (Pd atom labeled "$Pd^2_{ox,1}$" in Figure 11d−f) with concurrent backdonation from the Pd$_{ox}$ into the C−H bond, without concurrent changes in the valence of Pd$_{ox}$ centers. These early transition states result in a 0.138 nm C−H bond formed via heterolytic processes, in which the $CH_3^{\delta-}$ and H$^{\delta+}$ fragments are stabilized by Pd^{2+} and O^{2-}, respectively. The charge in the H-atom at the transition state (+0.411) is smaller than in the H of the OH* product (+0.670) or than in the transition state on O*−O* sites on 0.67 ML O* covered Pd(111) surfaces (+0.551, Figure 9). The negative charge in the CH_3 fragment at the transition state on PdO(101) (−0.148) reflects either direct heterolytic C−H splitting of the C−H bond along the reaction coordinate or concerted charge transfer within $(H_3C^{\delta-}\cdots Pd_{ox}\cdots H^{\delta+}\cdots O_{ox})^{\ddagger}$ complexes and stabilization of $H_3C^{\delta-}$ and H$^{\delta+}$ fragments by concerted

Table 3. Comparison of the Bader Charges on the Pd, C, O, and H Atoms As the Reaction Proceeds from the Reactant to the Transition State and to the Product State for the C−H Bond Activation of Methane on the Pd_{ox}−O_{ox} Site Pairs on the PdO(101) ($Pd^2_{ox,1}$−O^1_{ox} sites in Figure 1d) and PdO(100) ($Pd^1_{ox,1}$−O^1_{ox} sites in Figure 1c) Surfaces and on the Pd−O site Pairs on the 2/3 ML O*-Covered Pd(111) Surfaces (Pd−O sites in Figure 1b)

	PdO(101)			PdO(100)			2/3 ML O*/Pd(111)		
atom	reactant	transition state	product	reactant	transition state	product	reactant	transition state	product
Pd	+0.630	+0.644	+0.609	+0.880	+0.973	+1.022	+0.396	+0.620	+0.597
O	−0.744	−0.851	−1.112	−0.707	−0.827	−1.019	−0.592	−0.752	−0.995
C	−0.251	−0.455	−0.120	−0.160	−0.456	−0.240	−0.068	−0.489	−0.236
H	+0.083	+0.411	+0.726	+0.082	+0.403	+0.653	+0.038	+0.368	+0.628

interactions with Pd^{2+} and $H^{\delta+}$. The stabilization contrasts sharply the weak interactions between CH_3 and O* prevalent in the transition state for homolytic C−H activation on O*−O* pairs on Pd(111) surfaces (structure (**8b**), Figure 8). The extent of charge stabilization in these transition states differs: the CH_3 group in the transition state over PdO(101) is negatively charged (−0.148) and thus strongly interacts via Coulombic interactions with the positively charged Pd (+0.644) and H (+0.411) whereas the CH_3 group that forms in the transition state over O*-covered Pd(111) surfaces (**5b**) takes on free radical character with a charge of +0.13 and as such only weakly interacts with the resulting proton (with a charge of +0.55) that binds to O*. These effects of charge stabilization and structures at the transition state both influence the free energy of the transition state and, in turn, the activation barriers.

A Born−Haber thermochemical analysis allows C−H bond activation barriers ($\Delta E_{C-H,PdO}$) of methane on the stoichiometric Pd_{ox}−O_{ox} sites (labeled $Pd^2_{ox,1}$−O^1_{ox} in Figure 13a−c) at PdO(101) surfaces to be dissected into the energies of hypothetical steps, as shown in Figure 13, involving (i) homolytic C−H bond dissociation (BDE) of CH_4(g) into $CH_3^\bullet$ and $H^\bullet$ radicals (463 kJ mol⁻¹), (ii) the binding of $CH_3^\bullet$ on Pd_{ox} ($\Delta E_{Pd_{ox}-CH_3}$ = −238 kJ mol⁻¹), and (iii) the binding of $H^\bullet$ on O_{ox} ($\Delta E_{O_{ox}-H}$ = -164 kJ mol⁻¹) at PdO surfaces:

$$\Delta E_{C-H,PdO} = BDE + \Delta E_{Pd_{ox}-CH_3} + \Delta E_{O_{ox}-H} \qquad (3)$$

The stabilization of the CH_3 group by Pd_{ox} and through its residual bonding to H gives a binding energy $\Delta E_{Pd_{ox}-CH_3}$ of −238 kJ mol⁻¹ and a bond that is much stronger than for the CH_3 fragment on PdO(101) surfaces without concerted interactions with the vicinal H-atom (ΔE_{CH_3-PdO} = −125 kJ mol⁻¹, Table 2), as a result of electrostatic interactions between $H^{\delta+}$ and $CH_3^{\delta-}$ (Bader charges of +0.411 and −0.148, respectively, at the transition state, Figure 12). Such stabilization is evident from $(H_3C^{\delta-}\cdots Pd_{ox}\cdots H^{\delta+}\cdots O_{ox})^\ddagger$ transition states with a C−H bond distance (0.138 nm) much shorter than for C−H activation transition states on O*−O* or *−* site pairs (0.170 and 0.155 nm, respectively, Section 3.2). These strong interactions among O_{ox}, Pd_{ox}, C, and H atoms lead to tight transition states with fewer degrees of freedom and lower translational and rotational entropies than the transition states for C−H bond activation on O*−O* and *−* sites.

3.4. Comparison of C−H Bond Activation of Methane Over Pd−O Site Pairs on O*-Covered Pd, PdO(100), and PdO(101) Surfaces. The transition-state structures for CH_4 activation on Pd and oxygen site pairs (*−O* or Pd_{ox}−O_{ox}) on O*-covered Pd(111) (2/3 ML O*, Figure S2a, (**S2a.ii**)), PdO(100) (the $Pd^1_{ox,1}$−O^1_{ox} sites in Figure 11, (**11b**)), and PdO(101) ($Pd^2_{ox,1}$−O^1_{ox} sites in Figure 11, (**11e**)) show that

C−H activation occurs via mechanisms with common rearrangements reminiscent of σ-bond metathesis, but exhibiting subtle features responsible for their very different reactivities. C−H bond lengths in these three transition states [(**S2a.ii**), (**11b**), (**11e**)] are very similar (0.136−0.138 nm) and much shorter than in the transition states for the oxidative addition path (Figure 5, (**5b**), 0.155 nm). O−H bond lengths in the three transition-state structures are also small and similar (0.128−0.131 nm), consistent with O*-assisted C−H bond cleavage. Pd−CH_3 and Pd−H bonds are 0.009 and 0.027 nm shorter, respectively, on PdO(101) surfaces compared with those on O*-covered Pd(111), and both are ~0.010 nm shorter on the PdO(101) than those on PdO(100). These differences reflect repulsive interactions between CH_3 groups and vicinal O* on O*-covered Pd(111) and on PdO(100) surfaces as well as electronic interactions from the overoxidized (with structures resembling PdO_2, as described in Section 2.3) character of the nonstoichiometric PdO(100) surfaces.

A Born−Haber thermochemical cycle is used next to examine the different activation barriers on PdO(100) and PdO(101) surfaces (Table 2) and the charges in reactant, transition, and product states (Table 3). These results show that H-atom interactions with oxygen (O_{ox}) at the transition state are 34 kJ mol⁻¹ stronger on PdO(100) than on PdO(101) ($\Delta E_{O_{ox}-H}$ = −198 vs −164 kJ mol⁻¹), but CH_3 binding is much weaker ($\Delta E_{Pd_{ox}-CH_3}$ = −135 vs −238 kJ mol⁻¹). The weaker CH_3 binding is consistent with the longer Pd−CH_3 bonds on PdO(100) than on PdO(101) and with the weaker covalent character of the Pd−C bond on PdO(100). Previous studies have also shown that other species (e.g., H_2O) also bind on PdO(101) more strongly than on PdO(100).[24] Pd^{2+} centers in PdO(101) are formally $4d^8$ cations that can form bonds with significant covalent character,[24] thus allowing strong interactions with CH_4 and with the CH_3 and H fragments at the transition state. Table 3 shows that Pd_{ox} centers in PdO(100) are more positive than on PdO(101) in reactant, product, and transition states. These Pd_{ox} centers become even more positive in moving from reactants (+0.880) to transition states (+0.973), as electron density is transferred out of the surface and into the C−H bond. In contrast, the charge of Pd_{ox} centers (Pd^2_{ox} sites in Figure 1d) in PdO(101) remains essentially constant along the reaction coordinate (+0.630, reactant; +0.644, transition state).

These findings suggest that stoichiometric Pd^{2+}−$O^{2−}$ sites ($Pd^2_{ox,1}$−O^1_{ox} in Figure 1d) on PdO(101) provide the most effective acid−base pairs for heterolytic C−H activation, without concomitant charge transfer to the Pd_{ox} or O_{ox} species in the oxide. This process forms strong Pd⋯CH_3 and O⋯H interactions at the transition state. The balanced acid−base pairs of moderate strength in PdO(101) leads to facile

heterolytic bond cleavage, as proposed in the seminal work by Tanabe.[56,57] The higher barriers on PdO(100) reflect a requirement for charge transfer from Pd_{ox} into C−H bonds. Surfaces of PdO(100) are nonstoichiometric and resemble PdO_2,[50] consistent with the higher Pd_{ox} oxidation state in PdO(100) than in stoichiometric PdO(101) surfaces (+0.880 vs +0.630, Table 3). This leads to more basic O atoms but much weaker $Pd−CH_3$ interactions at the transition state and, as a result, to higher barriers on the more coordinatively saturated Pd−O sites on PdO(100) surfaces. Based on these results, C−H bond activation rate constants are estimated to be >10^3 larger on PdO(101) than PdO(100) surfaces at 873 K (assuming similar activation entropies).

3.5. Comparison of the Diverse C−H Bond Activation Pathways of Oxidative Addition, H-Abstraction, and σ-Bond Metathesis during Methane Oxidation on Uncovered Pd Metal, O*-Covered Pd Metal, and PdO Surfaces. Here, we compare measured and calculated activation enthalpies ($\Delta H^{\ddagger}$) and entropies ($\Delta S^{\ddagger}$), defined as their respective differences between the C−H activation transition states and gaseous CH_4, on Pd metal, O*-saturated Pd metal, and PdO cluster surfaces. These parameters define the activation free energies ($\Delta G^{\ddagger}$) within the framework of transition-state theory and are related to the C−H bond activation rate constant ($k_{C−H}$) according to

$$k_{C-H} = \frac{k_B T}{\hbar}\exp\left(-\frac{\Delta G^{\ddagger}}{RT}\right) = \frac{k_B T}{\hbar}\exp\left(-\frac{\Delta H^{\ddagger}}{RT} + \frac{\Delta S^{\ddagger}}{R}\right)$$

(4)

Here, k_B denotes the Boltzmann constant, $\hbar$ the Planck constant, and T the temperature.

C−H activation rate constants were measured on O*−O* and $Pd_{ox}−O_{ox}$ site pairs at 813−973 K on PdO and O* saturated Pd clusters (21.3 nm diameter); they are shown in Figure 14 together with those for reactions of $CH_4−H_2O/CO_2$ mixtures on *−* site pairs on bare Pd^0 clusters (12.5 nm mean diameter).[32] Activation enthalpies and entropies (by regression of C−H activation rate constants to the functional form of eq 4) are shown in Table 1 (and plotted in Figure 15) together with DFT-derived activation barriers.

Measured barriers are much higher on O*-saturated Pd^0 surfaces (158 kJ mol^{-1}) than on bare Pd metal or PdO surfaces (Pd^0: 84 kJ mol^{-1},[32] PdO: 61 kJ mol^{-1}), as also found by DFT methods (2/3 ML O* Pd(111): 145 kJ mol^{-1}, Pd(111): 73 kJ mol^{-1}, $Pd^2_{ox,1}−O^1_{ox}$ sites on PdO(101): 62 kJ mol^{-1}). The transition states on O*−O* pairs, $(O^*\cdots CH_3^{\bullet}\cdots ^*OH)^{\ddagger}$ (**8b**), involve essentially unbound radical-like $CH_3^{\bullet}$ fragments. In contrast, CH_3 and H fragments are both stabilized by their strong concerted interactions with Pd centers in the oxidative addition transition state, $(H_3C\cdots Pd\cdots H)^{\ddagger}$ (**5b**), on Pd^0 and in the σ-bond metathesis transition state, $(H_3C^{\delta-}\cdots Pd_{ox}\cdots H^{\delta+}\cdots O_{ox})^{\ddagger}$ (**11e**), on PdO(101) surfaces. The absence of O*$\cdots$H interaction in $(H_3C\cdots Pd\cdots H)^{\ddagger}$ (**5b**) transition states leads to higher C−H activation barriers [DFT: 73 kJ mol^{-1} on Pd(111) vs 62 kJ mol^{-1} on PdO(101), experimental: 84 kJ mol^{-1} (Pd^0) vs 61 kJ mol^{-1} (PdO), Table 1] and smaller measured rate constants on Pd^0 than on PdO catalysts (Figure 14).

The bond energies and distances between the oxygen and the leaving hydrogen in transition states and products reflect the extent of oxygen involvement in C−H bond activation on O*-covered Pd^0 and PdO surfaces. O−H bond lengths at the H-abstraction transition states, $(O^*\cdots CH_3^{\bullet}\cdots ^*OH)^{\ddagger}$ (**8b**),
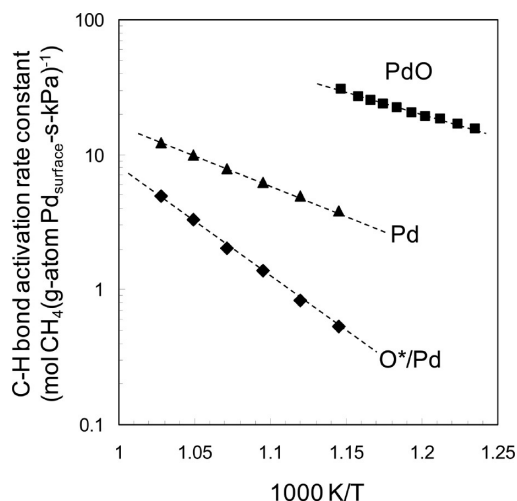
Figure 14. Temperature dependence of C−H bond activation rate constants on bare Pd metal clusters (▲), O* saturated Pd metal clusters (♦), and PdO clusters (■). (♦, ■: 0.2 % wt Pd/Al_2O_3; 21.3 nm mean Pd cluster diameter determined at the metallic state). PdO (■): 4.85 kPa CH_4, 72 kPa O_2, space velocity 3.92 × 10^9 cm^3 (s mol $Pd_{surface}$)$^{-1}$, 200 SiO_2/catalyst intraparticle dilution ratio, 1200 quartz/catalyst bed dilution ratio; oxygen saturated Pd metal (♦): rate data were taken from ref 9, 4.85 kPa CH_4, 1.2−1.6 kPa O_2, space velocity 9.40 × 10^8 cm^3 (s mol $Pd_{surface}$)$^{-1}$, 200 SiO_2/catalyst intraparticle dilution ratio, 280 quartz/catalyst bed dilution ratio; Pd metal (▲): rate data were taken from ref 32, which were measured on Pd clusters of 12.5 nm mean diameter supported on ZrO_2 (1.6 % wt Pd/ZrO_2)).
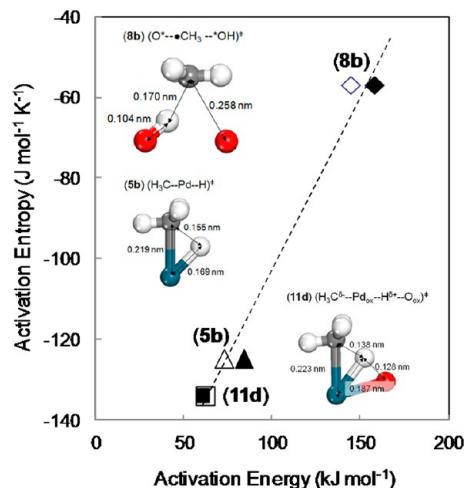
Figure 15. Correlation of the measured activation entropies and the measured (♦,▲,■) or DFT-derived (◇,△,□) activation barriers for C−H bond activation in CH_4 on Pd metal (▲,△), O*-covered Pd metal (♦,◇), and PdO (■,□). Kinetic parameters for Pd metal are derived from rate data reported in ref 32 and for O*-covered Pd metal and PdO are derived from the rate data in Figure 14.

resemble those of the hydroxyls in the products (0.104 vs 0.102 nm on O*-covered Pd^0) and are shorter than those at the σ-bond metathesis transition state $[(H_3C^{\delta-}\cdots Pd_{ox}\cdots H^{\delta+}\cdots O_{ox})^{\ddagger}$ (**11e**), 0.128 nm at the transition state and 0.098 nm in the product, on PdO(101)]. These results indicate that the enthalpy at the transition state is largely determined by the affinity of the O-atoms for H-atoms for the H-abstraction path and less so for the σ-bond metathesis path. This affinity of oxygen for H reflects the basicity of oxygen and is given by the energy differences between $O_{ox}H$ and O_{ox} on PdO surfaces

($\Delta E_{O_{ox}H-O_{ox}}$) and between OH* and O* on O*-saturated Pd^0 surfaces (ΔE_{OH*-O*}) at their stable structures and for the cases of oxygen adsorption energy [O_{ox} at PdO and O* at O* saturated Pd^0 surfaces], with H$^•$ at noninteracting distances. The interaction energies ($\Delta E_{O_{ox}H-O_{ox}}$) are slightly less negative on PdO(101) than on O*-saturated Pd(111) surfaces (−299 vs −321 kJ mol^{-1}, Table 2). These results suggest that the O_{ox}−H bonds (in the absence of the CH_3) are weaker than the O*−H bonds, thus, O_{ox} species on PdO(101) are less effective than O*-atoms at Pd^0 surfaces for H-abstraction. The lower H-abstraction reactivity on PdO surfaces is compensated by the strong $Pd_{ox}\cdots CH_3$ interactions at the transition state compared with those on O*-saturated Pd^0 surfaces, for which the CH_3 moieties are essentially at noninteracting distances from the O* species (0.258 nm).

Figure 15 shows measured activation energies and entropies on Pd^0, O* covered Pd^0, and PdO clusters as well as DFT-derived C−H bond activation barriers on Pd(111), O* saturated Pd(111), and PdO(101) surfaces. Entropy losses were largest on bulk PdO and smallest on O* saturated Pd^0 (−134 and −57 J mol^{-1} K^{-1}, respectively, Table 1). Measured activation entropies for the $(O*\cdots CH_3^•\cdots *OH)^‡$ (**8b**) transition state on O*−O* pairs (−57 J mol^{-1} K^{-1}) were much less negative than values expected from the loss of one translational mode at the transition state (−149 J mol^{-1} K^{-1}), because weakly bound CH_3 groups retain most of its translational freedom. The greater entropy losses as transition states evolve from $(O*\cdots CH_3^•\cdots *OH)^‡$ (**8b**), to $(H_3C\cdots Pd\cdots H)^‡$ (**5b**), and to $(H_3C^{\delta-}\cdots Pd_{ox}\cdots H^{\delta+}\cdots O_{ox})^‡$ (**11e**) are offset by greater enthalpic stabilization, brought forth by stronger interactions between CH_3 groups and Pd center, as depicted in Figure 15. The CH_3 moiety changes from an unbound state on O* covered Pd (**8b**), to three-center $(H_3C\cdots Pd\cdots H)^‡$ interactions on uncovered Pd^0 (**5b**), and ultimately to four-center $(H_3C^{\delta-}\cdots Pd_{ox}\cdots H^{\delta+}\cdots O_{ox})^‡$ structures (**11e**) on PdO(101). The extents of interaction of the CH_3 and H moieties with the active sites, basicities of reactive oxygen atoms, and accessibility of Pd atoms to CH_4 lead to mechanistically distinct C−H activation pathways of H-abstraction, oxidative addition, and σ-bond metathesis. The diverse transition-state structures and wide variation in activation energies and entropies of these pathways lead in turn to the marked differences in CH_4−O_2 rates among the metal, O* covered metal, and oxide structures.

4. CONCLUSIONS

Rate measurements in kinetically controlled regimes and DFT calculations were used to describe the diverse reaction paths and their associated catalytic requirements for C−H bond activation in CH_4 on Pd clusters with varying chemical states and surface oxygen coverages. The C−H bond of CH_4 cleaves over metal site pairs (*−*), oxygen site pairs (O*−O*), or Pd and oxygen ion site pairs (Pd_{ox}−O_{ox}) prevalent on Pd^0, oxygen-saturated Pd^0, or PdO cluster surfaces via oxidation addition, homolytic H-abstraction, or σ bond metathesis pathways, respectively. The activation energies and entropies differ markedly among these mechanistically distinct paths, because of distinction in enthalpic stabilization between the CH_3 and H moieties and the catalytic sites (*, O*, Pd_{ox}, or O_{ox}) and the extent of charge transfer at the transition states, as confirmed here from interpreting the activation enthalpy using Born–

Haber thermochemical cycle and Bader charge analysis along the reaction coordinate.

Metal atom site-pairs prevalent on uncovered Pd^0 clusters cleave the C−H bond by oxidative addition of one of the Pd atoms into the C−H bond, forming a three center transition state of $(H_3C\cdots Pd\cdots H)^‡$, before the transfer of H to another vicinal Pd site. Pd^0 cluster surfaces saturated with dense layer of chemisorbed oxygen atoms lack an accessible Pd^0 atom to interact with the CH_4 reactant and therefore cleave C−H bond homolytically using O*−O* sites via a H-abstraction step and the formation of free-radical-like methyl fragment in a high energy and entropy transition state $(O*\cdots CH_3^•\cdots *OH)^‡$. In contrast, PdO clusters (predominantly PdO(101) surfaces) expose both stoichiometric Pd_{ox} and O_{ox} ions that activate C−H bonds much more effectively than uncovered or O* saturated Pd^0 clusters in a concerted oxidative addition and reductive deprotonation route involving a tight, four-center transition state $[(H_3C\cdots Pd_{ox}\cdots H\cdots O_{ox})^‡]$.

The relative stability of the various transition-state structures $(H_3C\cdots Pd\cdots H)^‡$, $(O*\cdots CH_3^•\cdots *OH)^‡$, and $(H_3C\cdots Pd_{ox}\cdots H\cdots O_{ox})^‡$ is interpreted in terms of the catalytic function of oxygen and Pd and of the extent of charge transfer. The reactivity of oxygen on Pd^0 or PdO surfaces for H-abstraction is connected to their thermodynamic affinity toward the H. Lattice oxygen ions on PdO surfaces exhibit lower affinity toward H, interact more weakly with the H leaving group at the C−H activation transition state, and are therefore less effective for H-abstraction than the chemisorbed oxygen atoms on Pd^0 cluster surfaces. Their lower reactivity toward H-abstraction is compensated by the involvement of vicinal Pd ions in stabilizing the methyl fragments and charge transfer between the CH_3 and H moieties and the PdO cluster surfaces at the transition state, which in combination significantly stabilize the transition state on PdO over those on O* saturated or uncovered Pd surfaces. These diverse C−H bond activation routes and the catalytic functions of metal and ligand resemble those reported for organometallic complexes in homogeneous reactions. The reactivity of ligand (oxygen), accessibility of metal to CH_4 reactant, and the chemical states of Pd (and O) dictate the stability, extent of charge transfer between surfaces and CH_3 and H fragments, and charges at the C−H bond activation transition state. These differences in stabilities and charges influence the nature of C−H bond activation path and lead to distinct rates and kinetic parameters observed on bare Pd, O* saturated Pd, and PdO cluster surfaces.

■ ASSOCIATED CONTENT

Ⓢ Supporting Information

Oxygen saturation coverages. Effects of O* binding strength on the C−H activation barrier for C−H bond activation on Pd-oxygen atom (*−O*) site pairs on Pd(111) surfaces. This material is available free of charge via the Internet at http://pubs.acs.org.

■ AUTHOR INFORMATION

Corresponding Authors
iglesia@berkeley.edu
mn4n@virginia.edu

Notes

The authors declare no competing financial interest.

Article

■ REFERENCES

(1) Zhu, G.; Han, J.; Zemlyanov, D. Y.; Ribeiro, F. *J. Phys. Chem. B* **2005**, *109*, 2331.

(2) Wang, H.; Iglesia, E. *J. Catal.* **2010**, *273*, 245.

(3) Hensen, E. J. M.; Vissenberg, M. J.; de Beer, V. H. J.; van Veen, J. A. R.; van Santen, R. A. *J. Catal.* **1996**, *163*, 429.

(4) Hummel, A. A.; Wilson, A. P.; Delgass, W. N. *J. Catal.* **1988**, *113*, 236.

(5) McCarty, J. G. *Catal. Today* **1995**, *26*, 283.

(6) Datye, A. K.; Bravo, J.; Nelson, T. R.; Atanasova, P.; Lyubovsky, M.; Pfefferle, L. *Appl. Catal., A* **2000**, *198*, 179.

(7) Farrauto, R. J.; Hobson, M. C.; Kennelly, T.; Waterman, E. M. *Appl. Catal., A* **1992**, *81*, 227.

(8) Chin Y.-H.; García-Diéguez, M.; Iglesia, E. *J. Catal.* in preparation.

(9) Chin, Y.-H.; Iglesia, E. *J. Phys. Chem. C* **2011**, *115*, 17845.

(10) Chin, Y.-H.; Buda, C.; Neurock, M.; Iglesia, E. *J. Am. Chem. Soc.* **2011**, *133*, 15958.

(11) García-Diéguez, M.; Chin, Y.-H.; Iglesia, E. *J. Catal.* **2012**, *285*, 260.

(12) David, R. L. *Handbook of Chemistry and Physics*, 87th ed.; CRC Press: Boca Raton, FL, 2006.

(13) Koros, R. M.; Nowak, E. J. *Chem. Engr. Sci.* **1967**, *22*, 470.

(14) Kresse, G.; Hafner, J. *Phys. Rev. B* **1994**, *49*, 14251.

(15) Kresse, G.; Furthmuller, J. *Comput. Mater. Sci.* **1996**, *6*, 15.

(16) Kresse, G.; Furthmuller, J. *Phys. Rev. B* **1996**, *54*, 11169.

(17) Vanderbilt, D. *Phys. Rev. B* **1990**, *41*, 7892.

(18) Monkhorst, H. J.; Pack, J. D. *Phys. Rev. B* **1976**, *13*, 5188.

(19) Methfessel, M.; Paxton, A. *Phys. Rev. B* **1989**, *40*, 3616.

(20) Kittel, C. *Introduction to Solid State Physics*, 6th ed.; J. Wiley and Sons, Inc.: New York, 1986.

(21) Zheng, G.; Altman, E. I. *Surf. Sci.* **2000**, *462*, 151.

(22) Rogal, J.; Reuter, K.; Scheffler, M. *Phys. Rev. B* **2004**, *69*, 075421.

(23) Waser, J.; Levy, H. A.; Peterson, S. W. *Acta Crystallogr.* **1953**, *6*, 661.

(24) Kan, H. H.; Colmyer, R. J.; Asthagiri, A.; Weaver, J. F. *J. Phys. Chem. C* **2009**, *113*, 1495.

(25) Mills, G.; Jonsson, H.; Schenter, G. K. *Surf. Sci.* **1995**, *324*, 305.

(26) Henkelman, G.; Uberuaga, B. P.; Jonsson, H. *J. Chem. Phys.* **2000**, *113*, 9901.

(27) Henkelman, G.; Jonsson, H. *J. Chem. Phys.* **2000**, *113*, 9978.

(28) Sheppard, D.; Terrell, R.; Henkelman, G. *J. Chem. Phys.* **2008**, *128*, 134106.

(29) Bader, R. *Atoms in Molecules: A Quantum Theory*; Oxford University Press: New York, 1990; Henkelman, G.; Arnaldsson, A.; Jonsson, H. *Comput. Mater. Sci.* **2006**, *36*, 354.

(30) Stable CH_4 turnover rates were attained at extended reaction times (>80 ks) on both the metal and oxide clusters. Refer to ref 9 for the effects of time-on-stream on first-order rate constants during CH_4 oxidation on Pd metal cluster surfaces.

(31) Chin, Y.-H.; Buda, C.; Neurock, M.; Iglesia, E. *J. Catal.* **2011**, *283*, 10.

(32) Yamaguchi, A.; Iglesia, E. *J. Catal.* **2010**, *274*, 52.

(33) van Santen, R. A.; Neurock, M.; Shetty, S. G. *Chem. Rev.* **2010**, *110*, 2005.

(34) Ciobîcă, I. M.; Frechard, F.; van Santen, R. A.; Kleyn, A. W.; Hafner, J. *J. Phys. Chem. B* **2000**, *104*, 3364.

(35) Labinger, J. A.; Bercaw, J. E. *Nature* **2002**, *417*, 507.

(36) Cundari, T. R.; Grimes, T. V.; Gunnoe, T. B. *J. Am. Chem. Soc.* **2007**, *129*, 13172.

(37) Cundari, T. R. *J. Am. Chem. Soc.* **1994**, *116*, 340.

(38) Bunnik, B. S.; Kramer, G. J. *J. Catal.* **2006**, *242*, 309.

(39) Henkelman, G.; Jónsson, H. *Phys. Rev. Lett.* **2001**, *86*, 664.

(40) Jones, G.; Jakobsen, J. G.; Shim, S. S.; Kleis, J.; Andersson, M. P.; Rossmeisl, J.; Abild-Pedersen, F.; Bligaard, T.; Helveg, S.; Hinnemann, B.; Rostrup-Nielsen, J. R.; Chorkendorff, I.; Sehested, J.; Norskov, J. K. *J. Catal.* **2008**, *259*, 147.

(41) Biswas, B.; Sugimoto, M.; Sakaki, S. *Organometallics* **2000**, *19*, 3895−3908.

(42) Pallassana, V.; Neurock, M. *J. Catal.* **2000**, *191* (2), 301.

(43) van Santen, R. A.; Neurock, M. *Molecular Heterogeneous Catalysis: A Conceptual and Computational Approach*; Wiley-VCH: Weinheim, Germany, 2006; p 107.

(44) Dai, G.-L.; Liu, Z.-P.; Wang, W.-N.; Lu, J.; Fan, K.-N. *J. Phys. Chem. C* **2008**, *112*, 3719.

(45) Rozanska, X.; Fortrie, R.; Sauer, J. *J. Phys. Chem. C* **2007**, *111*, 6041.

(46) Madix, R. J.; Roberts, J.T. The Problem of Heterogeneously Catalyzed Partial Oxidation: Model Studies on Single Crystal Surfaces. In *Surface Reactions*, Madix, R.J., Ed.; Springer-Verlag: Berlin, 1994.

(47) Ayre, C. R.; Madix, R. J. *J. Am. Chem. Soc.* **1995**, *117*, 2301.

(48) Hellman, A.; Resta, A.; Martin, N. M.; Gustafson, J.; Trinchero, A.; Carlsson, P.-A.; Balmes, O.; Felici, R.; van Rijn, R.; Frenken, J. W. M.; Andersen, J. N.; Lundgren, E.; Grönbeck, H. *Phys. Chem. Lett.* **2012**, *3*, 678.

(49) Mayernick, A. D.; Janik, M. J. *J. Catal.* **2011**, *278*, 16.

(50) Blanco-Rey, M.; Jenkins, S. J. *J. Chem. Phys.* **2009**, *130*, 014705.

(51) Weaver, J. F.; Hinojosa, J. A., Jr.; Hakanoglu, C.; Antony, A.; Hawkins, J. M.; Asthagiri, A. *Catal. Today* **2011**, *160*, 213.

(52) Cummins, C. C.; Baxter, S. M.; Wolczanski, P. T. *J. Am. Chem. Soc.* **1988**, *110*, 8731.

(53) Cummins, C. C.; Schaller, C. P.; Van Duyne, G. D.; Wolczanski, P. T.; Chan, A. W. E.; Hoffmann, R. *J. Am. Chem. Soc.* **1991**, *113*, 2985.

(54) Oxgaard, J.; Muller, R. P.; Goddard, W. A.; Periana, R. A. *J. Am. Chem. Soc.* **2004**, *126*, 352.

(55) Cundari, T. R. *Organometallics* **1993**, *12*, 4971.

(56) Tanabe, K.; Yamaguchi, T. *Catal. Today* **1994**, *20*, 185.

(57) Tanabe, K. *Appl. Catal.* **1994**, *113*, 147.